

## Structure-based optimization of potent, selective and orally bioavailable CDK8 inhibitors discovered by high throughput screening

Paul Czodrowski, Aurélie Mallinger, Dirk Wienke, Christina Esdar, Oliver Poeschke, Michael Busch, Felix Rohdich, Suzanne A. Eccles, Maria Jesus Ortiz Ruiz, Richard Schneider, Florence I Raynaud, Paul A. Clarke, Djordje Musil, Daniel Schwarz, Trevor C Dale, Klaus Urbahns, Julian Blagg, and Kai Schiemann

*J. Med. Chem.*, **Just Accepted Manuscript** • DOI: 10.1021/acs.jmedchem.6b00597 • Publication Date (Web): 04 Aug 2016

Downloaded from <http://pubs.acs.org> on August 5, 2016

### Just Accepted

“Just Accepted” manuscripts have been peer-reviewed and accepted for publication. They are posted online prior to technical editing, formatting for publication and author proofing. The American Chemical Society provides “Just Accepted” as a free service to the research community to expedite the dissemination of scientific material as soon as possible after acceptance. “Just Accepted” manuscripts appear in full in PDF format accompanied by an HTML abstract. “Just Accepted” manuscripts have been fully peer reviewed, but should not be considered the official version of record. They are accessible to all readers and citable by the Digital Object Identifier (DOI®). “Just Accepted” is an optional service offered to authors. Therefore, the “Just Accepted” Web site may not include all articles that will be published in the journal. After a manuscript is technically edited and formatted, it will be removed from the “Just Accepted” Web site and published as an ASAP article. Note that technical editing may introduce minor changes to the manuscript text and/or graphics which could affect content, and all legal disclaimers and ethical guidelines that apply to the journal pertain. ACS cannot be held responsible for errors or consequences arising from the use of information contained in these “Just Accepted” manuscripts.

1  
2  
3 **Structure-based optimization of potent, selective and orally bioavailable**  
4  
5 **CDK8 inhibitors discovered by high throughput screening**  
6  
7  
8  
9  
10

11 Paul Czodrowski,<sup>\*(1)</sup> Aurélie Mallinger,<sup>(2)</sup> Dirk Wienke,<sup>(1)</sup> Christina Esdar,<sup>(1)</sup> Oliver Pöschke,<sup>(1)</sup> Michael  
12 Busch,<sup>(1)</sup> Felix Rohdich,<sup>(1)</sup> Suzanne A. Eccles,<sup>(2)</sup> Maria-Jesus Ortiz-Ruiz,<sup>(2)</sup> Richard Schneider,<sup>(1)</sup> Florence  
13 Raynaud,<sup>(2)</sup> Paul A. Clarke,<sup>(2)</sup> Djordje Musil,<sup>(1)</sup> Daniel Schwarz,<sup>(1)</sup> Trevor Dale,<sup>(3)</sup> Klaus Urbahns,<sup>(1)</sup> Julian  
14 Blagg,<sup>(2)</sup> and Kai Schiemann<sup>\*,(1)</sup>  
15  
16  
17  
18  
19

20  
21 (1) Merck KGaA, Darmstadt, 64293, Germany  
22

23  
24 (2) Cancer Research UK Cancer Therapeutics Unit at The Institute of Cancer Research, London, SW7  
25  
26 3RP, U.K.  
27

28  
29 (3) School of Bioscience, Cardiff University, Cardiff, CF10 3AX, U.K.  
30  
31

32  
33  
34  
35  
36 \* Corresponding authors: [paul.czodrowski@merckgroup.com](mailto:paul.czodrowski@merckgroup.com), [kai.schiemann@merckgroup.com](mailto:kai.schiemann@merckgroup.com)  
37  
38  
39  
40

41  
42 **ABSTRACT**  
43

44  
45 The Mediator complex-associated cyclin dependent kinase CDK8 regulates beta-catenin-  
46 dependent transcription following activation of WNT signaling. Multiple lines of evidence  
47 suggest CDK8 may act as an oncogene in the development of colorectal cancer. Here we  
48 describe the successful optimization of an imidazo-thiadiazole series of CDK8 inhibitors that  
49 was identified in a high-throughput screening campaign and further progressed by structure-  
50 based design. In several optimization cycles, we improved the microsomal stability, potency  
51  
52  
53  
54  
55  
56  
57  
58  
59  
60

1  
2  
3 and kinase selectivity. The initial imidazo-thiadiazole scaffold was replaced by a 3-methyl-1H-  
4  
5 pyrazolo[3,4-*b*]-pyridine which resulted in compound **25** (MSC2530818) that displayed  
6  
7 excellent kinase selectivity, biochemical and cellular potency, microsomal stability and is  
8  
9 orally bioavailable. Furthermore, we demonstrated modulation of phospho-STAT1, a  
10  
11 pharmacodynamic biomarker of CDK8 activity, and tumor growth inhibition in an *APC*-  
12  
13 mutant SW620 human colorectal carcinoma xenograft model after oral administration.  
14  
15 Compound **25** demonstrated suitable potency and selectivity to progress into preclinical in  
16  
17 vivo efficacy and safety studies.  
18  
19  
20  
21  
22  
23  
24  
25

## 26 INTRODUCTION

27  
28  
29 In contrast to other members of the CDK family (e.g. CDK1, CDK2 and CDK4/6), neither CDK8  
30  
31 nor its paralog CDK19 are required for the regulation of cell cycle progression. Instead, CDK8  
32  
33 and CDK19 together with MED12/12L and MED13/13L respectively form a regulatory kinase  
34  
35 module for the Mediator complex.<sup>1,2</sup> The Mediator complex is a large protein assembly that  
36  
37 couples gene-specific transcriptional regulators to the general RNA polymerase II  
38  
39 transcription machinery.<sup>2-7</sup> CDK8 and CDK19 participate in the regulation of transcription  
40  
41 through phosphorylation of RNA polymerase II<sup>8</sup> and other transcription factors to regulate  
42  
43 their activity or tag them for proteosomal degradation.<sup>9-14</sup>  
44  
45  
46  
47

48  
49 The role of CDK19 in cellular biology and human disease is not well understood and is the  
50  
51 subject of ongoing investigation.<sup>1</sup> However, in contrast, CDK8 is much better characterized  
52  
53 and has been proposed to act as an oncogene in colon cancer<sup>15</sup> and approximately 60 % of  
54  
55 colorectal cancers have increased *CDK8* gene copy number.<sup>16</sup> Moreover, a worse prognosis  
56  
57 in colon, breast and ovarian cancer is linked to increased CDK8 expression.<sup>17</sup> CDK8 is also  
58  
59  
60

1  
2  
3 essential for cell proliferation in melanoma.<sup>18</sup> Additional cancer-relevant activities of CDK8  
4  
5 include growth factor-induced transcription, modulation of TGF beta-signaling,<sup>13</sup> and  
6  
7 phosphorylation of the Notch intracellular domain.<sup>19,20</sup> Although knockout of CDK8 prevents  
8  
9 embryonic development due to its essential role in the pluripotent stem cell, other studies  
10  
11 have reported that CDK8 depletion does not affect the growth of normal cells.<sup>15,21,22</sup>  
12  
13

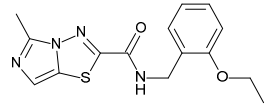
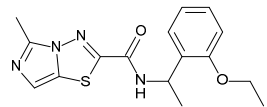
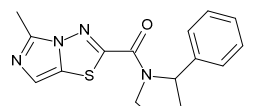
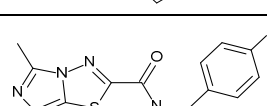
14  
15 CDK8 may also contribute to tumorigenesis through activation of beta-catenin regulated  
16  
17 gene expression,<sup>16</sup> a core transcriptional regulator of canonical WNT signaling. Consistent  
18  
19 with this observation, expression of the *CDK8* gene is correlated with activation of beta-  
20  
21 catenin in colon and gastric cancers.<sup>17,23</sup> Due to its involvement as a regulator of WNT/beta-  
22  
23 catenin signaling, CDK8 may be linked with disorders and diseases in which activation of  
24  
25 WNT/beta-catenin is crucial such as hyperproliferative, inflammatory or degenerative  
26  
27 disorders, and several malignant diseases.<sup>19,20</sup>  
28  
29  
30  
31

32  
33 An extensive contemporary review reports the current status of small molecule inhibitors for  
34  
35 CDK8/CDK19 and highlights an increasing interest in targeting CDK8;<sup>24</sup> in addition, a recent  
36  
37 report demonstrates a potential use for CDK8 inhibitors in AML.<sup>25</sup> We recently described the  
38  
39 discovery of small molecule inhibitors of CDK8 from a cell based high-throughput screen  
40  
41 (HTS) seeking WNT signaling inhibitors and also reported additional differentiated series of  
42  
43 CDK8 inhibitors from a scaffold-hopping approach using the biochemical screen reported  
44  
45 herein.<sup>26-30</sup> Here we describe the identification of a novel CDK8/19 chemotype from a  
46  
47 biochemical HTS versus CDK8 and its subsequent optimization, enabled by structure-based  
48  
49 design, to give compound **25**, a potent, selective and orally bioavailable CDK8/19 ligand  
50  
51 suitable for further progression into preclinical studies.  
52  
53  
54  
55  
56  
57  
58  
59  
60

## RESULTS & DISCUSSION

In a CDK8 high-throughput screen using a FRET-based Lanthascreen binding competition assay<sup>27</sup>, we identified several hit compounds with sub-micromolar activity. Our hit series contained an imidazo[5,1-*b*][1,3,4]thiadiazole scaffold, henceforth described as the “imidazo-thiadiazole” series. Initial hits bore either a 2-substituted benzyl substituent (**1** and **2**) or a 2-phenylpyrrolidine ring (**3** and **4**) attached to the imidazo-thiadiazole scaffold via an amide bond at the 2-position (Table 1). As a cellular readout of WNT signaling, we used our previously described 7dF3 WNT-specific reporter gene assay<sup>31</sup> and observed a 3- to 13-fold drop off from *in vitro* CDK8 binding affinity to cell-based activity for compounds **1 – 4**.

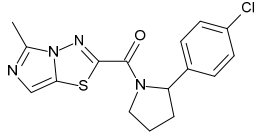
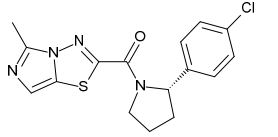
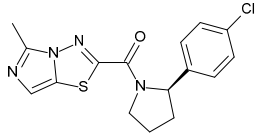
**Table 1** HTS hits from the “imidazo-thiadiazole” series

ID	Structure	CDK8 IC <sub>50</sub> [nM]	7dF3 IC <sub>50</sub> [nM]	CL <sub>int</sub> [μL/min/mg]		
				Human	Rat	Mouse
1		129 ± 27	1650 ± 495	>1000	435	119
2		781 ± 114	2450 ± 778	61	38	>1000
3		77 ± 4	415 ± 262	56	446	145
4		60 ± 6	290 ± 141	38	280	129

Introduction of a methyl group to the alkyl linker resulted in a 6-fold drop in biochemical potency (compound **2**, Table 1) and the pyrrolidine moiety was favored over an alkyl chain linker by virtue of significantly increased cell-based potency and improved metabolic stability

(compounds **3** and **4**). Hydrogen to fluorine exchange at the para position of the phenyl ring (compound **3** to **4**) did not influence biochemical nor cell-based potency; however, we noted a slight improvement in microsomal stability (Table 1). To further explore the impact of the para-substitution and stereochemistry at the pyrrolidine 2-position, the racemic form and both the enantiomers bearing a *p*-Cl-phenyl were synthesized (Table 2). The racemic form (**5**) showed modest biochemical and cell-based activity. Interestingly, the *S*-enantiomer (**6**) was significantly more active than the *R*-enantiomer (**7**); however, the microsomal stability of both enantiomers was in the same range.

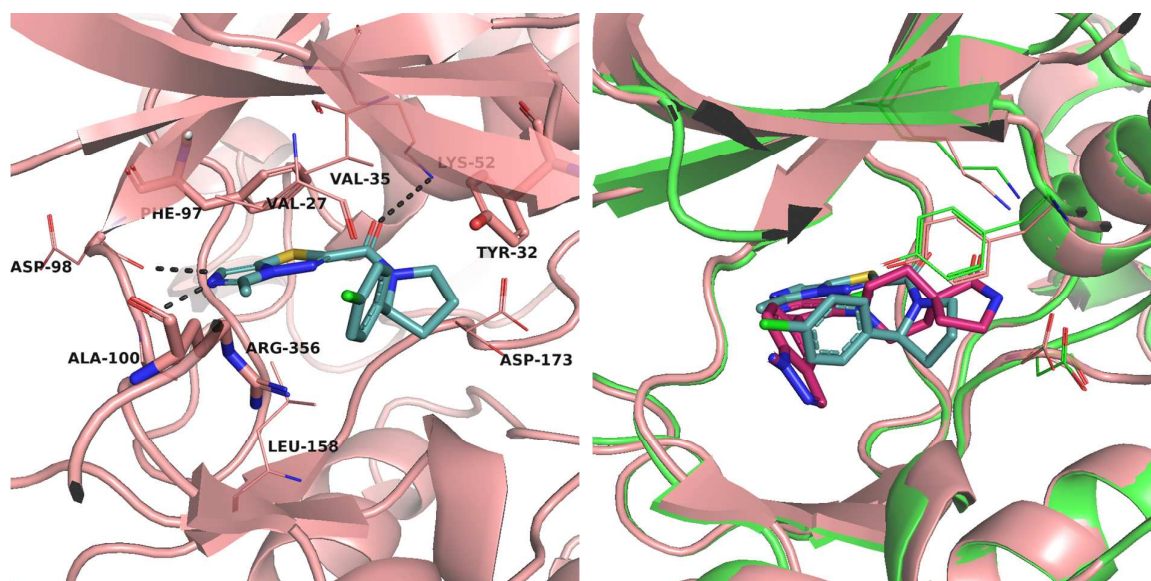
**Table 2** Determination of optimal pyrrolidine stereochemistry

ID	Structure	CDK8 IC <sub>50</sub> [nM]	7dF3 IC <sub>50</sub> [nM]	CL <sub>int</sub> [μL/min/mg]		
				Human	Rat	Mouse
5		17 ± 0.02	100 ± 28	52	719	388
6		3.8 ± 1.9	70 ± 14	49	655	447
7		110 ± 15	1,600 ± 0	60	449	514

In order to understand the binding mode and to inform further medicinal chemistry design, we determined the crystal structure of the most potent enantiomer (**6**) bound to CDK8/cyclin C (Figure 1A). Compound **6** is bound to the hinge region of CDK8 (Ala100) via the nitrogen atom at the 6-position of the “imidazo-thiadiazole” scaffold whilst the 5-methyl group points away from the gatekeeper residue (Phe97) towards the solvent-exposed

1  
2  
3 channel. The carbonyl group of the C2-amide forms a cation-pi interaction to the catalytic  
4  
5 lysine residue (Lys52), too distant (3.6 Å) to be considered as a hydrogen bond. The sulfur  
6  
7 atom of the “imidazo-thiadiazole” scaffold is positioned to form favorable van der Waals  
8  
9 (vdW) interactions to the gatekeeper residue Phe97. The pyrrolidine ring also forms  
10  
11 favorable vdW interactions to Tyr32 and the side chain of Asp173. Furthermore, the  
12  
13 orientation of the pyrrolidine defines the exit vector for the *p*-Cl-phenyl substituent which  
14  
15 itself forms vdW interactions with Val27, Tyr32, Val35, Leu158 and Arg356. We did not  
16  
17 observe sufficient evidence to support a halogen bond between the chlorine atom and the  
18  
19 backbone C=O of Val27: the distance is 2.9 Å and the angle between the chlorine atom and  
20  
21 the C=O functionality of Val27 is 104.7°.  
22  
23  
24  
25  
26  
27  
28  
29

30 Comparison of the structure of **6** in CDK8/cyclin C with our recently published crystal  
31  
32 structure of a 3,4,5-trisubstituted-2-aminopyridine chemotype<sup>27</sup> (compound **8**, CCT251921)  
33  
34 revealed few structural differences in the active site. The CDK8 residues in the ATP binding  
35  
36 site with the largest variance between the two crystal structures are shown (**Figure 1B**).  
37  
38 Despite the different modes of ligand-binding, the protein structure is largely conserved.  
39  
40 Compound **6** and compound **8**<sup>27</sup> both form H-bond acceptor interactions with the backbone  
41  
42 NH of hinge residue Ala100 and interact with the catalytic lysine (Lys52) through the amide  
43  
44 and lactam carbonyl groups respectively. However, interaction with the gatekeeper residue  
45  
46 Phe97 is mediated by the sulfur atom of the thiadiazole scaffold **6** as opposed to the 3-  
47  
48 chlorosubstituent in compound **8**. Most notably, the para-chlorophenyl and *N*-  
49  
50 methylindazole rings that project into a similar region in the CDK8 solvent channel are linked  
51  
52 to the hinge-binding scaffold through different architectures in the two series (**Figure 1B**).  
53  
54  
55  
56  
57  
58  
59  
60



(A)

(B)

**Figure 1 (A)** Crystal structure of CDK8/cyclin C complexed with compound **6** (blue). Hydrogen bonds are displayed as dashed lines. The cation-dipole interaction between the carbonyl atom and the catalytic Lys52 is also shown. The key amino acids are given in stick representation. **(B)** Alignment of compound **6** (blue)/CDK8/cyclin C crystal structure (salmon) and compound **8** (pink)/CDK8/cyclin C crystal structure (green). The residues which deviate most are highlighted: Tyr32, Lys52, and Asp173.



1  
2  
3 We were concerned that the thiadiazole ring may be prone to oxidative metabolism and  
4  
5 therefore set out to discover a modified scaffold hop in order to mitigate this risk. In  
6  
7 addition, we wished to explore variation of the pyrrolidine ring and its pendant 2-phenyl  
8  
9 substituent in order to optimize potency and metabolic stability.  
10  
11

### 12 13 **(1) Scaffold hop from the hinge binding motif of the "imidazo-thiadiazole" series** 14 15

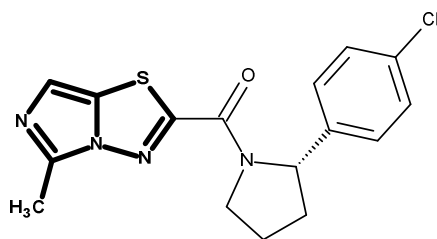
16 We modified the "imidazo-thiadiazole" scaffold based upon the crystal structure of  
17  
18 compound **6** in CDK8/cyclinC (**Figure 1A**) according to SZMAP<sup>32</sup> and WaterMap<sup>33</sup> analysis  
19  
20 (see **Figure 2**). We ran these calculations for the ligand-deleted form of the crystal structure  
21  
22 of compound **6** with CDK8/cyclin C. Given this calculation set-up, we could analyze the  
23  
24 energy of predicted water sites inside the hinge binding region and identify possible handles  
25  
26 for scaffold variations.  
27  
28

29  
30  
31 SZMAP [Solvent ZAP (ZAP is a Poisson-Boltzmann solver) MAPping] represents a mixture of  
32  
33 an implicit and explicit solvent model. In brief, a grid with a spacing of 0.25 Å is generated  
34  
35 inside the protein active site and an explicit water molecule is positioned at each grid point  
36  
37 with multiple orientations, followed by an implicit solvent Poisson-Boltzmann  
38  
39 calculation.<sup>34,35</sup> These calculations can be done with and without the ligand. For our analysis,  
40  
41 we performed the calculations without the ligand. Once the calculations are completed for  
42  
43 all grid points, an overall energy grid for the presence or absence of water molecules is  
44  
45 computed. The predicted water molecules show different characteristics based on their  
46  
47 energy values: a water molecule is characterized as "hydrophobic" if its energy value is  
48  
49 positive, otherwise it is characterized as "hydrophilic".  
50  
51  
52  
53  
54

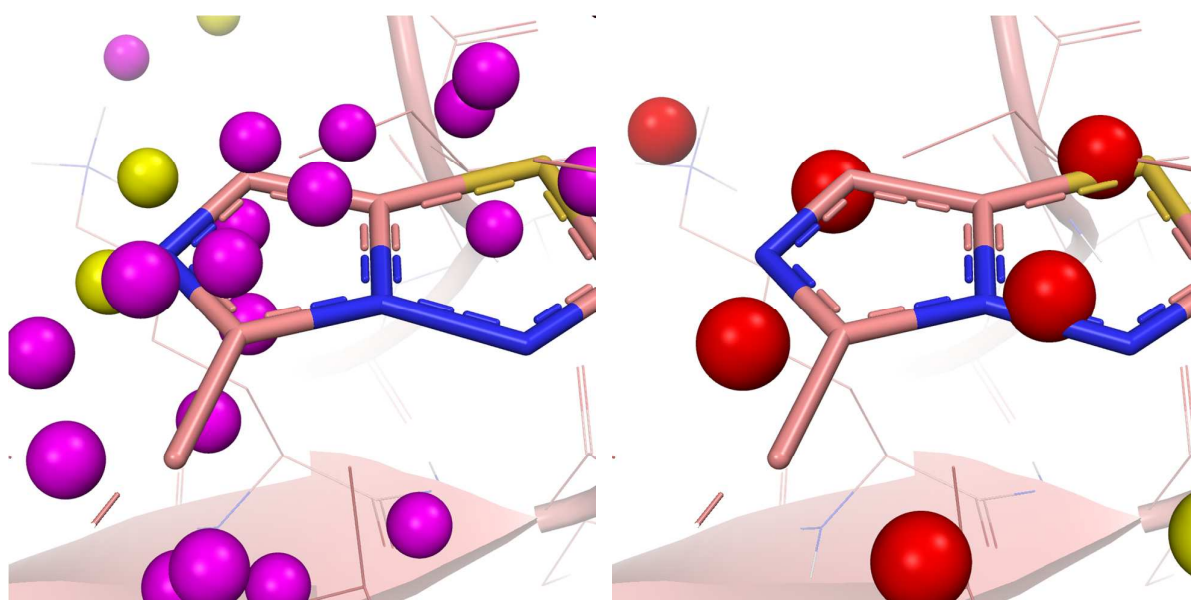
55  
56 The WaterMap methodology is a combination of MD simulation<sup>36</sup> with the Inhomogeneous  
57  
58 Fluid Approach<sup>37</sup>. In brief, this approach calculates the enthalpic and entropic contributions  
59  
60

1  
2  
3 of binding per predicted water molecule. Consistent with the SZMAP analysis, the ligand was  
4  
5 left out for the WaterMap calculations. If the overall free energy per predicted water  
6  
7 molecule is positive, it is specified as "unhappy water", whereas a predicted negative free  
8  
9 energy indicates a "happy water".  
10

11  
12  
13 The interpretation of SZMAP and WaterMap calculations can be used for the differentiation  
14  
15 of binding modes observed for highly structurally-related ligands<sup>38</sup> and for rationalization of  
16  
17 SAR,<sup>39,40</sup> kinase selectivity,<sup>41</sup> and binding kinetics.<sup>42</sup> In the course of our studies, we  
18  
19 employed SZMAP and WaterMap for the interpretation of modifications to the hinge binding  
20  
21 scaffold. Applying these computational approaches, we explored changes to the five-  
22  
23 membered ring of the hinge binding motif and selected a range of 5,6-bicyclic scaffolds for  
24  
25 synthesis. The remainder of the molecule was fixed by the *S*- *p*-Cl-2-phenyl-pyrrolidine motif  
26  
27  
28  
29  
30 (**Table 3**) and compounds were scored by WaterMap, see **Figure 2(C)**.  
31  
32  
33  
34  
35  
36  
37  
38  
39  
40  
41  
42  
43  
44  
45  
46  
47  
48  
49  
50  
51  
52  
53  
54  
55  
56  
57  
58  
59  
60



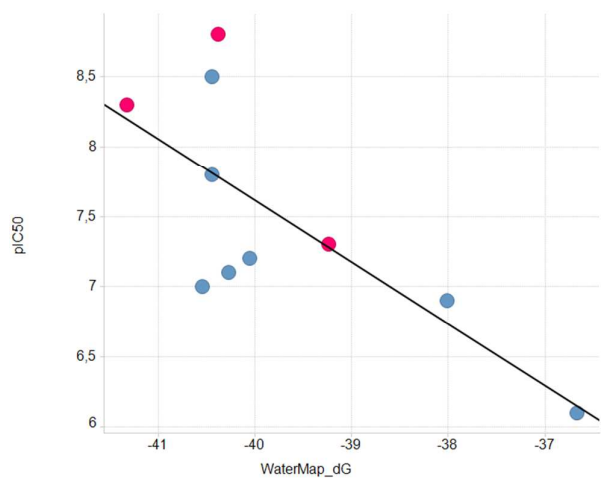
(A)



(B)

(C)

**Figure 2** (A) SZMAP and WaterMap calculations have been performed for the crystal structure of compound **6** complexed to CDK8/cyclin C. For clarity, only part of the ligand denoted in bold (Figure



1  
2  
3 **2A)** is shown in Figures **2(B)** and **2(C)**. **(B) Upper panel:** Only the hinge region is shown. SZMAP  
4  
5 analysis of the CDK8/compound **6** crystal structure: yellow spheres correspond to water sites bearing  
6  
7 hydrophilic character and pink spheres correspond to water sites bearing hydrophobic character.  
8  
9 **Lower panel:** The contribution from each ligand atom resulting from water molecule replacement at  
10  
11 the same position is shown. The character of the ligand-displaced water spheres are depicted as  
12  
13 mesh: yellow mesh corresponds to hydrophilic water spheres, green mesh corresponds to  
14  
15 hydrophobic water spheres. The size of the water spheres correspond to the relative energy gain  
16  
17 obtained by replacement of the particular water sphere by each ligand atom. **(C) Upper panel:** Only  
18  
19 the hinge region is shown for clarity - the full ligand is depicted in Figure **2(A)** WaterMap analysis of  
20  
21 the CDK8/compound **6** crystal structure: red spheres correspond to “unhappy” water molecules,  
22  
23 yellow spheres to “happy” water molecules. **Lower panel:** WaterMap scoring versus CDK8 pIC<sub>50</sub> for  
24  
25 the compounds from Table 1 & 2 (blue dots) and the compounds from Table 3 (red dots),  $r^2 = 0.54$ .  
26  
27  
28  
29  
30  
31  
32

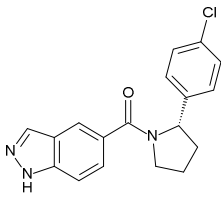
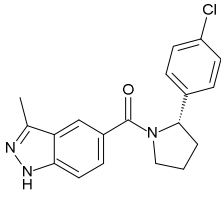
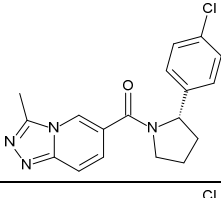
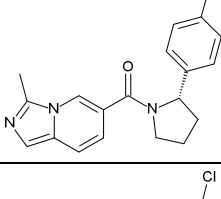
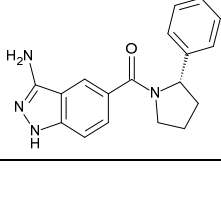
33 Analysis of the predicted water sites via SZMAP (see **Figure 2(B)**) revealed that hydrophilic  
34  
35 water molecules are favored directly adjacent to the hinge residues Ala100 and Asp98. This  
36  
37 is consistent with the corresponding hydrophilic hinge-binding motifs of our selected  
38  
39 scaffold replacements. The remaining part of the hinge binding region is predicted to be  
40  
41 mostly filled with hydrophobic water molecules. Such water molecules can be replaced by  
42  
43 both hydrophobic and hydrophilic moieties.<sup>43–45</sup> Based on this finding, we ranked our  
44  
45 compound ideas by WaterMap scores. In addition, the characterization of predicted water  
46  
47 sites by SZMAP calculations revealed that broad scaffold variations should be possible. The  
48  
49 new compound design ideas were also prioritized based upon their synthetic arose from  
50  
51 chemical tractability and their potential for improved primarily aimed for the optimization of  
52  
53 microsomal stability. Figure **2(B)** (lower panel) depicts the contribution from each ligand  
54  
55 atom resulting from water molecule replacement at the same position. This analysis  
56  
57  
58  
59  
60

underscores the 30-fold difference in CDK8 affinity between compounds **9** and **10**: the favorable binding contribution by addition of a methyl group at the 5-position is driven by the replacement of an “unhappy” water molecule; this finding is consistent with both the WaterMap and SZMAP predictions. Indeed, the WaterMap calculations (see **Figure 2(C)**) indicate that the hinge-binding region is filled with “unhappy” water molecules. We performed a ranking of our compounds based on the WaterMap scores for the docking solutions of compounds from Tables 1 & 2 which adopt a similar hinge-binding mode. Based on an acceptable trend between WaterMap scores and  $pIC_{50}$ , we also scored new compound ideas from Table 3. The outcome of this ranking is given in **Figure 2C** (lower panel) suggesting a weak correlation between the WaterMap-based analysis and the in vitro potency of compounds from Table 3. We omitted compound **11** from this analysis, because we anticipate a different binding mode; indeed, a 440-fold decrease in potency was seen with the introduction of an  $sp^2$  nitrogen atom juxtaposed to the C=O backbone group of Asp98, see compound **11**, versus the corresponding hydrogen bond donor in compound **10** (**Table 3**). However, compound **11** showed good microsomal stability indicating that an appropriate scaffold hop could significantly improve stability to oxidative metabolism. Pleasingly, the introduction of a methyl group at the 3-position of the indazole **9** to give **10** resulted in a 22-fold improvement in biochemical potency and a 166-fold increase in cell-based potency; however, no improvement in microsomal stability was observed consistent with the increased lipophilicity of compound **10** versus **9**.

In summary, the potency increase arising from introduction of the C3- methyl group in compound **10** is consistent with our SZMAP analysis (**Figure 2(B)**). However, we recognized that the indazole C3-methyl group could be susceptible to oxidative metabolism and therefore introduced a more polar amino group at this position (compound **13**) cognizant

that improved hinge-binding interaction with the backbone carbonyl of Ala100 may also be realized (**Figure 1**). This tactic maintained *in vitro* CDK8 potency and improved microsomal stability as desired but unfortunately led to a 47-fold drop in cellular potency – compared to compound **10** – despite good Caco2 flux ( $Papp_{A-B} = 33.7 \times 10^{-6} \text{ cm s}^{-1}$ ) and low efflux ratio (2.2).

**Table 3** Variation of the hinge binding motif of the “imidazo-thiadiazole” HTS scaffold

ID	Structure	CDK8 IC <sub>50</sub> [nM]	7dF3 IC <sub>50</sub> [nM]	CL <sub>int</sub> [μL/min/mg]		
				Human	Rat	Mouse
9		32 ± 33	100 ± 28	354	94	86
10		1.4 ± 0.1	0.6 ± 0.004	525	79	244
11		3,990 ± 1,151	>10,000	<10	19	18
12		9 ± 1	90 ± 14	390	108	63
13		4.9 ± 0.5	28 ± 3	23	10	10

1  
2  
3 Compound **13** proved optimal in terms of biochemical potency and metabolic stability and  
4  
5 was further profiled in a broad kinase panel to discover any kinase selectivity issues  
6  
7 (Supplementary Material Table S2). Five off-kinases were detected (JAK1, JAK2, JAK3, ROCK-  
8  
9 II and TYK2) and were subject to IC<sub>50</sub> determination to confirm potency (Table 4).  
10  
11  
12 Consequently, we aimed to improve selectivity versus these off-target kinases in subsequent  
13  
14 medicinal chemistry optimization.  
15  
16  
17

18 **Table 4** Kinase profile data for **13** (see also Supplementary Material, Table 2), sorted  
19  
20 alphabetically  
21  
22

kinase	IC <sub>50</sub> (nM)	% inhibition at 1 μM
CDK8	4.9	100
JAK1	90	86
JAK2	286	84
JAK3	219	79
ROCK-II	1,330	42
TYK2	279	70

23  
24  
25  
26  
27  
28  
29  
30  
31  
32  
33  
34  
35  
36  
37

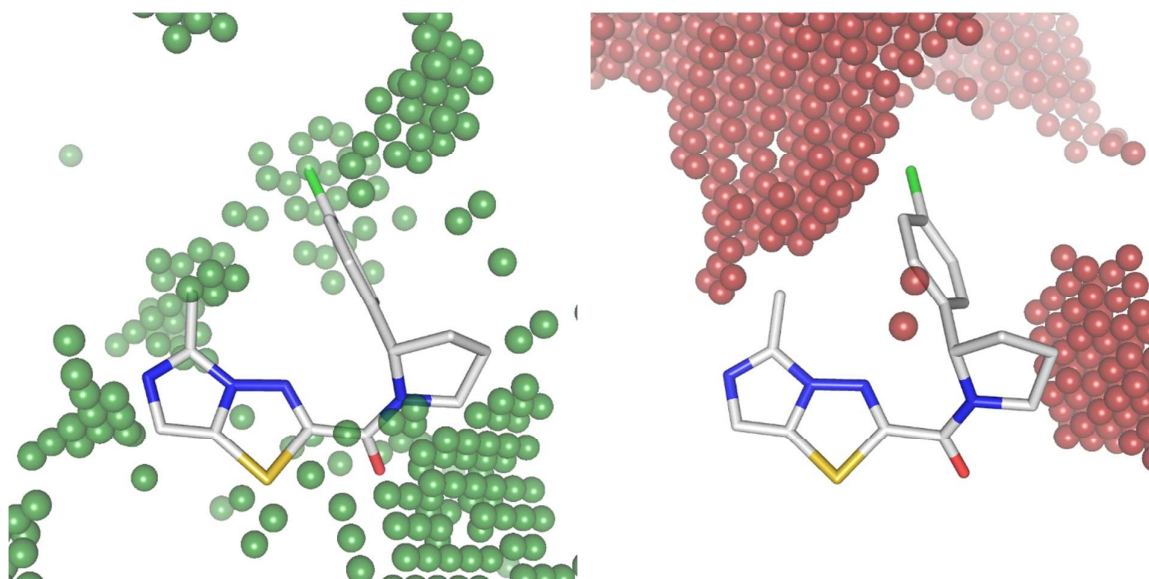
## 38 (2) Variation of the ring linker size and halogen substituents

39

40 In order to inform our medicinal chemistry design, we calculated Selectivity Grids<sup>46</sup> for the  
41  
42 CDK8/compound **6** crystal structure, see **Figure 3(A)**, and selectivity grids for the most  
43  
44 notable off-target kinases, see **Figure 3(B)**. Selectivity grids represent a plausible  
45  
46 interpretation of regions within binding pockets which may be targeted to improve (or to  
47  
48 lose) selectivity.<sup>46</sup> These selectivity grids suggested that the *para*-halogen substituent of the  
49  
50 phenyl ring and the 3-amino group of the indazole scaffold represented possible variation  
51  
52 points to achieve selectivity for CDK8 over the off-target kinases, see **Figure 3(A)**.  
53  
54  
55

56 Furthermore, this analysis suggested that substitution at the solvent-exposed region of the  
57  
58  
59  
60

1  
2  
3 binding pocket would non-specifically increase potency against the off-target kinases, see  
4  
5 **Figure 3(B)**. Therefore, we decided to vary the *para*-halogen substituent as well as the  
6  
7 pyrrolidine ring and also to methylate the 3-amino group on the indazole scaffold in order to  
8  
9 improve the selectivity and cell-based activity of compound **13** (**Table 5**).



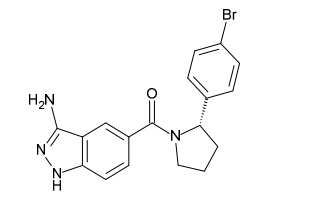
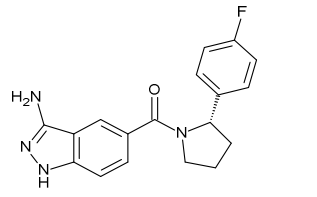
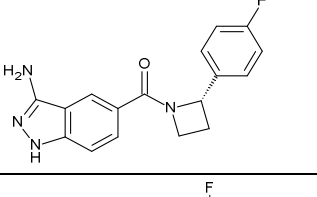
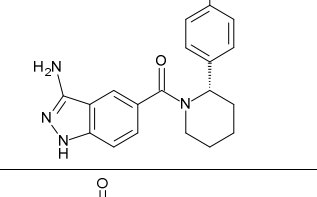
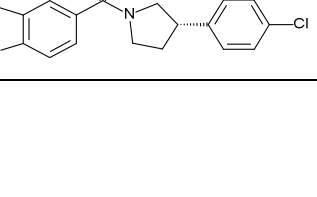
(A)

(B)

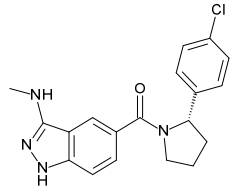
34  
35  
36  
37 **Figure 3 (A)** Selectivity Grids for the CDK8-specific regions of the active site. In general,  
38 regions around the *para*-substituted halogen in the phenyl ring as well as the region  
39 adjacent to the pyrrolidine ring can be considered as potential selectivity handles. **(B)**  
40  
41  
42 Selectivity Grids of the ATP binding pocket which have the potential to drive increased  
43  
44  
45  
46  
47  
48  
49  
50  
51  
52  
53  
54  
55  
56  
57  
58  
59  
60  
60 potency for off-target kinases such as the JAK family.



**Table 5** Variations of the ring linker size and *para*-substitution of the phenyl ring.

ID	Structure	CDK8	JAK1	JAK2	JAK3	ROCK-II	TYK2	CDK8	7dF3	CL <sub>int</sub> [μL/min/mg]		
		% inhibition at 1 μM						IC <sub>50</sub> [nM]		Human	Rat	Mouse
14		98	88	88	76	65	76	3.1 ± 1	19 ± 4	<10	<10	14
15		93	72	59	58	27	62	32 ± 0.4	120 ± 14	<10	<10	<10
16		94	63	24	21	12	45	49 ± 6	435 ± 163	10	<10	10
17		95	21	-2	-14	22	17	45 ± 3	800 ± 283	<10	15	28
18		96	24	-14	15	20	23	24 ± 6	150 ± 14	<10	26	19

1  
2  
3  
4  
5  
6  
7  
8  
9  
10  
11  
12  
13  
14  
15  
16  
17  
18  
19  
20  
21  
22  
23  
24  
25  
26  
27  
28  
29  
30  
31  
32  
33  
34  
35  
36  
37  
38  
39  
40  
41  
42  
43  
44  
45  
46  
47  
48  
49

19		99	34	34	37	17	32	5.4 ± 3	12 ± 6	18	28	31
----	---	----	----	----	----	----	----	---------	--------	----	----	----

1  
2  
3 The kinase selectivity data confirmed the hypothesis that the *para*-substituent could act as  
4  
5 selectivity handle: The %\_INHIBITION values, which refer to single point measurements of  
6  
7 percent inhibition at 1  $\mu$ M, demonstrate that the off-target activity versus the JAK family  
8  
9 decreases as the *para*-halogen substituent is varied from Br to Cl to F. Selectivity could be  
10  
11 further improved by modifications of the ring linker size or switching from a 1,2-substitution  
12  
13 pattern to a 1,3-substitution pattern of the pyrrolidine linker. Pleasingly, the affinity for off-  
14  
15 target kinases was also reduced by methylating the 3-amino group.  
16  
17  
18  
19  
20  
21  
22

23  
24 In summary, variation of the halogen substituent in the *para*-position of the phenyl ring  
25  
26 showed a clear trend – while the on-target biochemical CDK8 and cellular 7dF3 potencies  
27  
28 decreased from Br to Cl to F in the matched trio **14**, **13**, and **15**; less potent off-target activity  
29  
30 versus the JAK family, ROCK-II and TYK2 was also observed. Interestingly, all three  
31  
32 compounds were metabolically stable. Replacement of pyrrolidine (**15**) with azetidine (**16**)  
33  
34 retained biochemical potency and microsomal stability with slight loss in cell-based potency.  
35  
36 The same held true when increasing the ring size from a pyrrolidine to a piperidine linker  
37  
38 (**17**) although cell-based potency was further eroded. Alteration of the substitution pattern  
39  
40 at the pyrrolidine from 1,2 to 1,3 showed a moderate loss of biochemical and cellular  
41  
42 potency (compare **18** with **13**) while maintaining good microsomal stability. Finally, the  
43  
44 addition of a methyl group to the 3-amino functionality of the indazole scaffold resulted in  
45  
46 equipotent biochemical and cellular activity (compare **19** with **13**) combined with a slight  
47  
48 loss of microsomal stability.  
49  
50  
51  
52  
53  
54  
55  
56  
57  
58  
59  
60

1  
2  
3 We next determined the crystal structure of compound **17** bound to CDK8/cyclin C (**Figure**  
4 **4A**) and examined the superposition of **17** with compound **6** (**Figure 4B**). The indazole hinge  
5 binding motif is located at the same position as the "imidazo-thiadiazole" scaffold of **6**. The  
6 N-atom in the 1-position of the indazole scaffold forms an additional hydrogen bond to the  
7 C=O backbone of Asp98 which cannot be formed by **6**. The carbonyl moiety linking the para-  
8 halo -phenyl piperidine to the hinge binding scaffold is located at the same position in both  
9 ligands. Interestingly, the exocyclic amino group in the 3-position of the indazole does not  
10 form a hydrogen bond with the backbone carbonyl atom of Ala100 (the heavy atom distance  
11 = 3.4 Å) and the electron density surrounding this amino group is not consistent with the  
12 placement of a water molecule. These observations are consistent with SZMAP and  
13 WaterMap calculations that did not predict an energetically favorable water molecule in this  
14 region. Compound **6** was 12-fold more potent than **17** versus CDK8 and we reasoned that  
15 this difference may be driven by the halogen substituent; indeed comparison of the matched  
16 molecular pair **15** and **17**, which only differ by the ring linker size (pyrrolidine vs piperidine),  
17 were equipotent (32 nM vs 45 nM). Although the ring size is increased from a 5-membered  
18 pyrrolidine linker to a 6-membered piperidine linker, the *p*-F phenyl ring is placed at an  
19 almost identical position compared to compound **6**, see **Figure 4(B)**. Comparing the fluorine  
20 atom (compound **17**) to the chlorine atom (compound **6**), the halogen to Val27 carbonyl  
21 distance is increased from 2.9 Å (compound **6**, chlorine) to 3.7 Å (compound **17**, fluorine).  
22 We observed only one other structural difference: the distance between the carbonyl linker  
23 and the catalytic lysine Lys52 (3.6 Å for compound **6** and 4.6 Å for compound **17**). Thus, we  
24 attribute the increased potency of compound **6** to the improved interaction of the *para*-Cl  
25 atom with Val27 compared to the *para*-F atom in compound **17** together with improved  
26 interaction between the carbonyl linker and Lys52 for compound **6**.  
27  
28  
29  
30  
31  
32  
33  
34  
35  
36  
37  
38  
39  
40  
41  
42  
43  
44  
45  
46  
47  
48  
49  
50  
51  
52  
53  
54  
55  
56  
57  
58  
59  
60

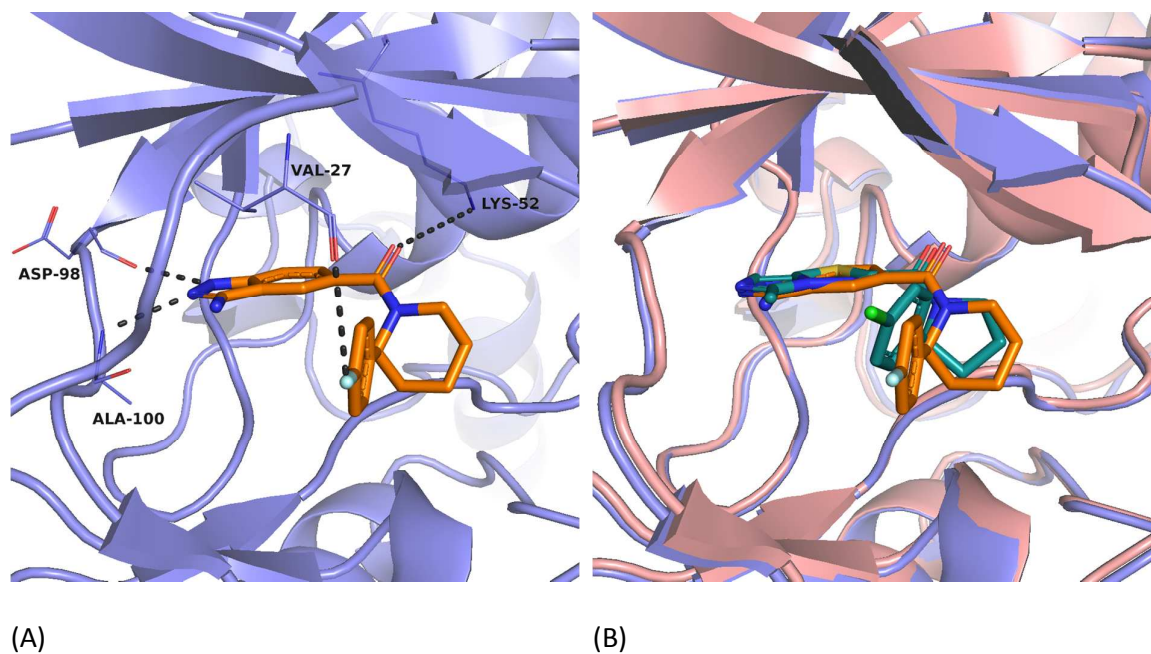


**FIGURE 4 (A)** Crystal structure of **17** (orange) in complex CDK8/cyclin C. The hydrogen bonds are indicated by black dotted lines. **(B)** Superposition of crystal structures of compounds **17** (orange) and **6** (blue).

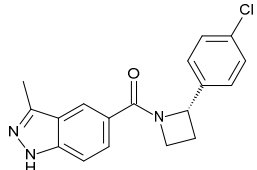
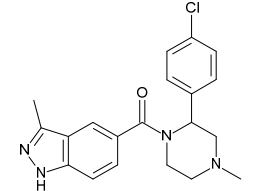
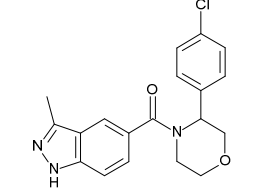
Although we had improved the kinase selectivity and maintained microsomal stability by variations of the pyrrolidine linker and *para*-halogen substituent, the resultant compounds (**16** and **17**) lacked the desired biochemical potency and cellular activity. Comparison of the matched molecular pair C3-amino with C3-methyl (**13** vs **10**), indicated that the C3-methyl substitution resulted in good cellular potency, albeit with poorer microsomal stability. Consequently, we selected the C3-methylindazole scaffold for further progression.

### (3) Optimization of microsomal stability

In vitro metabolite identification studies indicated that the pyrrolidine ring linker is the major site of oxidative metabolism for compound **10**. Thus, we prepared close analogues of compound **10** with reduced overall lipophilicity with the aim of improving metabolic stability (**Table 6**).

Replacement of the pyrrolidine by an azetidine (compound **20**) did not lead to improved metabolic stability in all species; however the racemic piperazine and morpholine derivatives (**21** and **22** respectively) resulted in improved  $CL_{int}$  profiles across all species; disappointingly, we observed a decrease in the biochemical CDK8 affinity and the cellular potency (**Table 6**).

**Table 6** Variations of the ring linker size based on the 3-methyl-indazole scaffold.

ID	Structure	CDK8 IC <sub>50</sub> [nM]	7dF3 IC <sub>50</sub> [nM]	CL <sub>int</sub> [μL/min/mg]		
				Human	Rat	Mouse
20		1.7 ± 0.1	2.0 ± 0.4	908	62	113
21		15 ± 2	230 ± 14	135	40	63
22		8.5 ± 2	115 ± 7	135	44	29

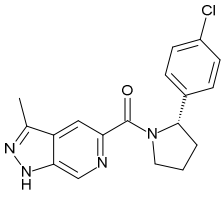
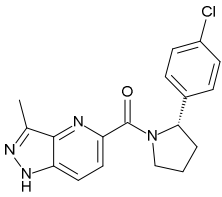
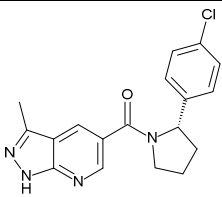
1  
2  
3 In summary, the microsomal stability could be improved by reducing overall lipophilicity;  
4  
5 however, a corresponding drop in biochemical and cell-based activity was also observed.  
6  
7 Therefore we attempted to improve the metabolic stability by reducing the lipophilicity of  
8  
9 the molecule through the introduction of polarity into the hinge-binding scaffold.  
10  
11  
12  
13  
14  
15

#### 16 **(4) Fine-Tuning of the hinge binding motif**

17  
18

19 The pyrazole hinge binding motif was fixed and the six-membered ring of the indazole  
20  
21 scaffold was varied by introduction of single nitrogen atoms in the 4-, 6- and 7-positions to  
22  
23 reduce the overall lipophilicity of the scaffold (compounds **23** to **25**, **Table 7**). Introduction of  
24  
25 a nitrogen atom at the 5-position of the indazole ring (**23**) resulted in a significant drop in  
26  
27 biochemical and cell-based potency. Nitrogen at the 4-position of the indazole ring gave the  
28  
29 most potent analog (**24**); however, this compound showed only modest microsomal stability.  
30  
31 Pleasingly, introduction of a nitrogen atom at the 7-position (**25**) resulted in acceptable  
32  
33 biochemical CDK8 affinity and furthermore showed improved microsomal stability (**Table 7**).  
34  
35  
36  
37  
38  
39  
40  
41  
42  
43  
44  
45  
46  
47  
48  
49  
50  
51  
52  
53  
54  
55  
56  
57  
58  
59  
60

**Table 7** Fine-tuning of the hinge binding motif.

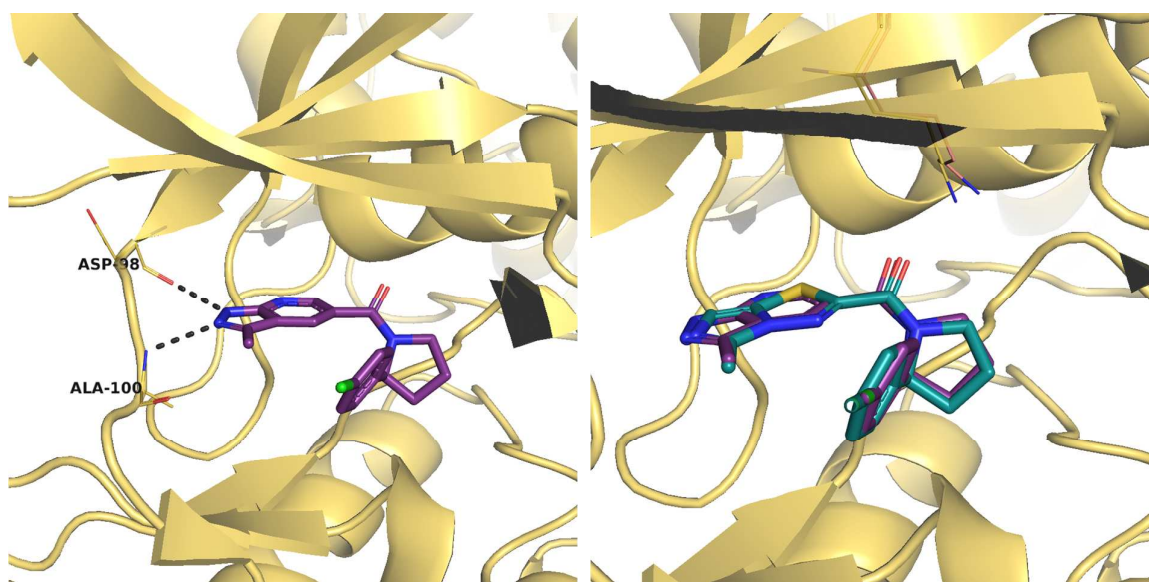
ID	Structure	CDK8 IC <sub>50</sub> [nM]	7dF3 IC <sub>50</sub> [nM]	CL <sub>int</sub> [μL/min/mg]		
				Human	Rat	Mouse
23		11 ± 1.6	125 ± 35	206	70	61
24		1.3 ± 0.06	2.8 ± 0.4	100	69	29
25		2.6 ± 0.1	6.5 ± 2	45	<10	<10

The matched molecular pair compound **25** versus compound **6**, where only the hinge binding scaffold (“pyrazolo-pyridine” vs. “imidazo-thiadiazole”) has been changed, showed equivalent biochemical CDK8 affinity and a 11-fold improvement in cell-based potency together with a significant improvement in mouse and rat microsomal stability.

We next determined the crystal structure of **25** bound to CDK8/cyclin C (**Figure 5A**). The carbonyl atom at C5 of the azaindazole scaffold of **25** forms a hydrogen bond to Lys52 and the side-chain of Lys52 moves towards the ligand in comparison to the binding mode of compound **6** in CDK8/cyclin C (**Figure 5B**). Overall, the orientation of the active site residues is well conserved between the crystal structures of **25** and **6**. The interaction pattern is identical except for an additional favorable interaction from the *N*1-indazole hydrogen bond donor to the backbone C=O atom of Asp98 for **25**. Notably, the additional nitrogen atom at



1  
2  
3 the 7-position of the indazole scaffold does not elicit any additional favorable interactions  
4  
5 consistent with the corresponding biochemical potencies: indazole **10** (CDK8 IC<sub>50</sub> = 1.4 nM)  
6  
7  
8 versus aza-indazole **25** (CDK8 IC<sub>50</sub> = 2.6 nM).  
9  
10  
11  
12  
13  
14  
15  
16  
17  
18  
19  
20  
21  
22  
23  
24  
25  
26  
27  
28  
29  
30  
31  
32



(A)

(B)

33  
34  
35  
36 **Figure 5 (A)** Crystal structure of **25** (violet) complexed with CDK8-cyclin C **(B)** Superposition  
37  
38 of the **25** (violet) and **6** (blue) crystal structures  
39  
40  
41  
42  
43

44 In a commercially available reporter displacement assay,<sup>47</sup> compound **25** binds to CDK8 and  
45 CDK19 with similar affinity (4 nM) - as we have previously observed across multiple  
46 chemotypes<sup>27-30</sup> - with residence times of 18 and 32 min respectively. Potent inhibition of  
47 phospho-STAT1<sup>SER727</sup>, an established biomarker of CDK8 activity,<sup>26</sup> in SW620 human  
48 colorectal carcinoma cells was also observed (pSTAT1<sup>SER727</sup> IC<sub>50</sub> = 8 ± 2 nM). Furthermore,  
49 compound **25** demonstrated potent inhibition of WNT-dependent transcription in human  
50 cancer cell lines that have constitutively activated WNT signalling; for example, **25** inhibited  
51  
52  
53  
54  
55  
56  
57  
58  
59  
60

24

1  
2  
3 the reporter-based luciferase readout in several cell lines bearing activating WNT-pathway  
4  
5 mutations; LS174T (*beta-catenin*-mutant,  $IC_{50} = 32 \pm 7$  nM), COLO205 (*APC*-mutant,  $IC_{50} = 9 \pm$   
6  
7 1 nM) and demonstrated inhibition of WNT3a ligand-dependent reporter readout in PA-1  
8  
9 cells ( $IC_{50} = 52 \pm 30$  nM). Compound **25** demonstrated minimal activity in the CEREP panel,  
10  
11 being active on the dopamine transporter ( $IC_{50} = 8.5$   $\mu$ M) as the only activity below 10  $\mu$ M,  
12  
13 and demonstrated minimal hERG inhibition (18%@10uM). Testing against a 264 kinase panel  
14  
15 gave inhibition of only a single kinase by more than 50% at 1  $\mu$ M (GSK3alpha  $IC_{50} = 700$ ).  
16  
17 Furthermore, compound **25** is a soluble CDK8 inhibitor (kinetic solubility >200  $\mu$ M,  
18  
19 thermodynamic solubilities: 0.399 mg/mL (PBS, pH 7.4), 0.628 mg/mL (FaSSIF, pH 6.5) and  
20  
21 0.836 mg/mL (FeSSIF, pH 5.0)) with high permeability ( $P_{appA-B} = 44 \times 10^{-6}$   $cm^2 s^{-1}$ ) and low  
22  
23 efflux ratio in Caco-2 cells (ER = 1.5) and does not inhibit any cytochrome P450 subtypes  
24  
25 (Cyp  $IC_{50}$ s > 20  $\mu$ M). In light of its promising in vitro profile, **25** was further profiled in in vivo  
26  
27 pharmacokinetic and pharmacological studies. Overall, the compound showed acceptable  
28  
29 pharmacokinetics (PK) in all tested preclinical species (**Table 8**). Prediction of the human PK  
30  
31 was performed by three species allometric scaling corrected for protein binding and  
32  
33 considering interspecies-differences in intrinsic clearance in liver microsomes. The human  
34  
35 clearance (CL) and volume of distribution at steady-state ( $V_{ss}$ ) were estimated to be low  
36  
37 ( $\sim 0.14$  L/h/kg) and small (0.48 L/kg), respectively, resulting in a short predicted terminal half-  
38  
39 life (2.4 h). Physiological based pharmacokinetics (PBPK) simulations suggested that human  
40  
41 oral bioavailability may be  $\geq 75\%$  up to dose level of 500 mg daily.  
42  
43  
44  
45  
46  
47  
48  
49  
50  
51  
52  
53  
54  
55  
56  
57  
58  
59  
60

**Table 8:** Pharmacokinetic profile of compound **25**

Species	$f_u$ (%)	$V_{D_{SS}}$ (L/kg)	Plasma Cl (L/h/kg)	%Qh	$t_{1/2}$ (h)	F
Mouse	13%	0.59	1.37	22.5	0.45	0.25
Rat	19%	1.62	1.50	34.6	0.86	0.66
Dog	50%	1.47	1.35	53.8	0.83	0.39
Human Prediction	16%	~0.48	~0.14	12.1	~2.4	>0.75*

\* Predicted by PBPK modeling (GastroPlus™)

Compound **25** was then assessed *in vivo* in an established SW620 human colorectal cancer xenograft model in female NCr athymic mice. Tumor-bearing mice were treated orally with compound **25** (50 mg/kg bid or 100 mg/kg qd), for 16 days. Both schedules gave a similar reduction in tumor growth (**Figure 6 (A)**) with T/C ratios (based on final tumor weights) of 49% and 57% respectively. The compound was generally well tolerated, with no effects on mouse body weight in the q.d. administration schedule and manageable body weight loss with the bid schedule (**Figure 6 (B)**). We monitored inhibition of STAT1<sup>SER727</sup> phosphorylation by a Luminex immunoassay; phospho-STAT1<sup>SER727</sup> levels were reduced to the limits of detection 2 h after dosing in both administration schedules and remained below the control levels even after 24 h, having more pronounced effects in the bid compared with the q.d. schedule (**Figure 6 (C)**).

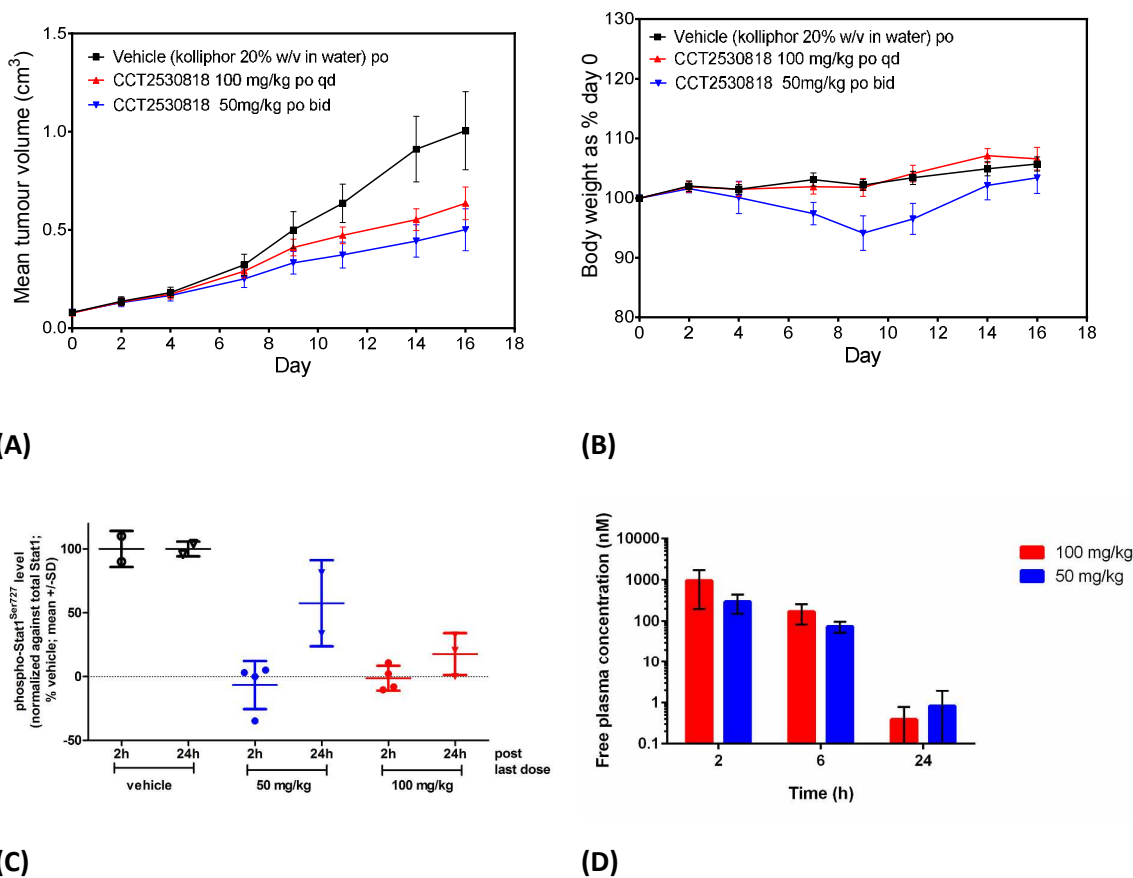


**Figure 6** Efficacy study of compound **25** in SW620 human colorectal cancer xenografts: (A) Tumor growth rates expressed as volumes (mean±SEM). (B) Mouse body weights expressed as % of day 0 values. (C) Phospho-STAT1<sup>SER727</sup> levels relative to total STAT1 levels and expressed as % vehicle controls at each time point. (D) Free plasma concentrations of compound **25** over time at the two dose schedules (50 mg/kg bid or 100 mg/kg q.d.),

## CONCLUSIONS

In an HTS campaign using a FRET-based Lanthascreen binding competition assay, we identified a chemical series comprising an imidazo-thiadiazole scaffold with exemplar compounds demonstrating IC<sub>50</sub> values in the 60 – 780 nM range (**Table 1**); however, this

1  
2  
3 series lacked sufficient microsomal stability. Determination of the crystal structure of  
4  
5 compound **6** in CDK8/cyclin C demonstrated clear differences in binding mode compared to  
6  
7 our previously reported 3,4,5 trisubstituted-2-aminopyridine series.<sup>27</sup> SZMAP and WaterMap  
8  
9 calculations were applied to identify potential scaffold replacements to enhance potency  
10  
11 and improve metabolic stability. Applying these computational approaches, we explored  
12  
13 changes to the skeleton of the five-membered ring of the imidazo-thiadiazole hinge binding  
14  
15 motif and discovered a series of indazole-based scaffold replacements. Notably, 3-methyl  
16  
17 indazole **10** demonstrated potent biochemical and cell-based potency; however insufficient  
18  
19 metabolic stability precluded further progression. Replacement of the C3-methyl substituent  
20  
21 with a C3-amino group gave compound **13** which demonstrated optimal biochemical  
22  
23 potency and metabolic stability but suffered from undesirable off-target kinase affinity.  
24  
25  
26  
27  
28

29  
30 We employed selectivity grids to rationalize key regions for the modulation of kinase  
31  
32 selectivity for the three most notable off-target kinases JAK1, JAK2, JAK3 and TYK2 and  
33  
34 discovered that selectivity could be improved by modifications to the pyrrolidine ring and by  
35  
36 variation of the para-halogen substituent on the pendant phenyl ring to give, for example,  
37  
38 the selective and metabolically stable para-fluorophenylpiperidine analog **17**. Crystallization  
39  
40 of **17** in CDK8/Cyclin C revealed a conserved binding mode; however, **17** lacked the desired  
41  
42 biochemical potency and cellular activity.  
43  
44  
45

46  
47 Revisiting the C3-methylindazole series and applying the principle of reduced lipophilicity to  
48  
49 abrogate oxidative metabolism, enabled the synthesis of potent and selective analogues  
50  
51 with improved cell-based potency compared to 3-amino-indazole **17**. In particular, the 7-  
52  
53 azaindole scaffold exemplified by compound **25** which demonstrated an optimal  
54  
55 compromise of biochemical and cell-based potency coupled with acceptable *in vitro*  
56  
57 metabolic stability that resulted in a favorable *in vivo* oral pharmacokinetic profile in mouse,  
58  
59  
60

1  
2  
3 rat and dog. Compound **25** demonstrated reduction of tumor growth rates of established  
4  
5 human SW620 colorectal carcinoma xenografts using two different oral dosing schedules.  
6  
7 We observed concomitant inhibition of a target engagement biomarker phospho-STAT1<sup>SER727</sup>  
8  
9 consistent with pharmacokinetic exposure.  
10

11  
12  
13 In light of its potent and selective profile coupled with good oral pharmacokinetics and  
14  
15 duration of *in vivo* target engagement on oral dosing, compound **25** (MSC2530818) was  
16  
17 selected for progression into further preclinical *in vivo* animal efficacy and safety studies.  
18  
19

## 20 21 **EXPERIMENTAL SECTION**

### 22 23 24 **Chemistry.**

25  
26  
27 Commercially available starting materials, reagents and dry solvents were used as supplied.  
28

29  
30 Column chromatography was performed on a CombiFlash Companion purification system  
31  
32 using Teledyne Isco silica cartridges. Preparative TLC was performed on Merck plates.  
33

34  
35 Preparative HPLC was conducted according the following methods: Method A, injections of  
36  
37 the sample were made onto a SunFire C18 OBD column (100 Å, 5 µm, 30 mm x 100 mm).  
38

39  
40 Chromatographic separation at room temperature was carried out using Agilent

41  
42 Technologies, 1260 Infinity, acetonitrile:water gradient (both modified with 0.1% trifluoro  
43  
44 acetic acid) at a flow rate of 50 mL/min. Chiral preparative HPLC was conducted according

45  
46 the following methods: Method B: Injections of the sample were made onto a ChiralPak AD-  
47  
48 H column (5 µm, 4.6 X 250 mm). Chiral chromatographic separation was carried at room

49  
50 temperature out using SFC Berger Minigram, CO<sub>2</sub>/Methanol (85:15) + 0.5% diethyl amine, at  
51  
52 a flow rate of 5 mL/min. Method C: Injections of the sample were made onto a ChiralPak AS-

53  
54 H column (5 µm, 4.6 X 250 mm). Chiral chromatographic separation was carried at room  
55  
56 temperature out using SFC Berger Minigram, CO<sub>2</sub>/Methanol (60:40), modified with 0.5%  
57  
58  
59  
60

1  
2  
3 diethyl amine, at a flow rate of 5 mL/min. Method D: Injections of the sample were made  
4  
5 onto a ChiralPak AD-H column (5  $\mu$ m, 4.6 X 250 mm). Chiral chromatographic separation was  
6  
7 carried at room temperature out using SFC Berger Minigram, CO<sub>2</sub>/Methanol (75:25) + 0.5%  
8  
9 diethyl amine, at a flow rate of 5 mL/min. Additional methods are directly describes in the  
10  
11 procedures. <sup>1</sup>H NMR spectra were recorded on a Bruker Avance-500, Bruker Avance 400,  
12  
13 Avance II 400 or Avance 300. Samples were prepared as solutions in a deuterated solvent  
14  
15 and referenced to the appropriate internal non-deuterated solvent peak. <sup>13</sup>C NMR spectra  
16  
17 were recorded at 101 MHz using an internal deuterium lock. The following internal  
18  
19 references were used: CDCl<sub>3</sub>, CD<sub>3</sub>OD and DMSO-d<sub>6</sub>; LC/MS and HRMS analysis was  
20  
21 performed on an Agilent 1200 series HPLC and diode array detector coupled to a 6210 time  
22  
23 of flight mass spectrometer with dual multimode APCI/ESI source. Analytical separation was  
24  
25 carried out according to the following Method: Method E, analytical separation was carried  
26  
27 out on a Chromolith® Speed ROD column (RP-18e, 50 x 4.6 mm) using a flow rate of 2.4  
28  
29 mL/min in a 3.9 min gradient elution with detection at 220 nm. The mobile phase was a  
30  
31 mixture of water containing 0.05% formic acid (solvent A) and acetonitrile containing 0.04%  
32  
33 formic acid (solvent B). Gradient elution was as follows: 95:5 (A/B) to 0:100 (A/B) over 2.8  
34  
35 min, 0:100 (A/B) for 0.5 min, and then reversion back to 95:5 (A/B) over 0.1 min, finally 95:5  
36  
37 (A/B) for 0.5 min; LC/MS and HRMS analysis was also performed on a SHIMADZU LC-MS  
38  
39 machine consisting of an UFLC 20-AD system with a LC-20 AD pump, SPD-M20A UV detector  
40  
41 and a LCMS 2020 MS detector; Method F, analytical separation was carried out on a Shim-  
42  
43 pack XR-ODS, column (2.2  $\mu$ M, 3.0 x 50 mm) using a flow rate of 1.0 mL/min in a 3.6 min  
44  
45 gradient elution with detection at 220 nm. The mobile phase was a mixture of water (solvent  
46  
47 A) and acetonitrile (solvent B) both containing 0.05% TFA. Gradient elution was as follows:  
48  
49 95:5 (A/B) over 0.01 min, then 95:5 to 0:100 (A/B) over 2.2 min, 0:100 (A/B) for 1.0 min, and  
50  
51  
52  
53  
54  
55  
56  
57  
58  
59  
60

1  
2  
3 then reversion back to 99:5 (A/B) over 0.1 min; method G, analytical separation was carried  
4  
5 out on a Shim-pack VP-ODS, column (2.2  $\mu$ M, 3.0 x 50 mm) using a flow rate of 1.0 mL/min in  
6  
7 a 5.6 min gradient elution with detection at 220 nm. The mobile phase was a mixture of  
8  
9 water (solvent A) and acetonitrile (solvent B) both containing 0.05% TFA. Gradient elution  
10  
11 was as follows: 95:5 (A/B) over 0.01 min, then 95:5 to 0:100 (A/B) over 4.2 min, 0:100 (A/B)  
12  
13 for 1.0 min, and then reversion back to 99:5 (A/B) over 0.1 min. Method H: LC/MS and HRMS  
14  
15 analysis was performed on a Waters Acquity UPLC and diode array detector coupled to a  
16  
17 Waters G2 QToF mass spectrometer fitted with a multimode ESI/APCI source. Analytical  
18  
19 separation was carried out at 30°C on a Phenomenex Kinetex XB-C18 column (30 x 2.1 mm,  
20  
21 1.7 $\mu$ , 100A) using a flow rate of 0.5 mL/min in a 2 minute gradient elution with detection at  
22  
23 254 nm. The mobile phase was a mixture of methanol (solvent A) and water (solvent B), both  
24  
25 containing formic acid at 0.1%. Gradient elution was as follows: 10:90 (A/B) to 90:10 (A/B)  
26  
27 over 1.25 min, 90:10 (A/B) for 0.5 min, and then reversion back to 10:90 (A/B) over 0.15 min,  
28  
29 finally 10:90 (A/B) for 0.1 min. Method I: LC/MS and HRMS analysis was performed on an  
30  
31 Agilent 1200 series HPLC and diode array detector coupled to a 6210 time of flight mass  
32  
33 spectrometer with dual multimode APCI/ESI source. Analytical separation was carried out at  
34  
35 30°C on a Merck Purospher STAR column (RP-18e, 30 x 4 mm) using a flow rate of 1.5  
36  
37 mL/min in a 4 minute gradient elution with detection at 254 nm. The mobile phase was a  
38  
39 mixture of methanol (solvent A) and water (solvent B), both containing formic acid at 0.1%.  
40  
41 Gradient elution was as follows: 10:90 (A/B) to 90:10 (A/B) over 2.5 min, 90:10 (A/B) for 1  
42  
43 min, and then reversion back to 10:90 (A/B) over 0.3 min, finally 10:90 (A/B) for 0.2 min. The  
44  
45 following references masses were used for HRMS analysis: caffeine [M+H]<sup>+</sup> 195.087652;  
46  
47 (hexakis(1H,1H,3H-tetrafluoropentoxy)phosphazene [M+H]<sup>+</sup> 922.009798) and hexakis(2,2-  
48  
49 difluoroethoxy)phosphazene [M+H]<sup>+</sup> 622.02896 or reserpine [M+H]<sup>+</sup> 609.280657. All  
50  
51  
52  
53  
54  
55  
56  
57  
58  
59  
60



1  
2  
3 compounds submitted for biological testing were determined to be >95% pure by Methods  
4  
5 E, F or G unless stated otherwise.  
6  
7  
8  
9

10  
11 The synthesis of the two key compounds **13** and **25** will be described in the following. The  
12  
13 synthesis of the remaining compounds can be found in the Supplementary Material.  
14  
15  
16  
17  
18  
19

20 **(13)** (3-amino-1*H*-indazol-5-yl)-[(2*S*)-2-(4-chlorophenyl)pyrrolidin-1-yl]methanone  
21

22  
23 To a solution of 3-amino-1*H*-indazole-5-carboxylic acid (50 mg, 0.28 mmol), 2-(4-chloro-  
24  
25 phenyl)-pyrrolidine hydrochloride (123 mg, 0.560 mmol) and 4-methylmorpholine (0.060 mL,  
26  
27 0.58 mmol) in *N,N*-dimethyl-formamide (2 mL) were added *O*-(1*H*-benzotriazol-1-yl)-  
28  
29 *N,N,N',N'*-tetramethyluroniumtetrafluoroborate (TBTU, 83 mg, 0.26 mmol) and 1-  
30  
31 hydroxybenzotriazole hydrate (HOBT, 9 mg, 0.07 mmol). The reaction mixture was stirred at  
32  
33 RT for 15 h. Water was added to the mixture and the resulting precipitate was filtered off  
34  
35 and dried in vacuo. The crude product was purified by prep. HPLC (method A,  
36  
37 acetonitrile/water) to yield in 48 mg (50%) of (3-amino-1*H*-indazol-5-yl)-[2-(4-  
38  
39 chlorophenyl)pyrrolidin-1-yl]methanone as a yellow solid. <sup>1</sup>H NMR (400 MHz, DMSO-*d*<sub>6</sub>) δ  
40  
41 11.70-11.38 (m, 1H), 8.31-7.74 (m, 1H), 7.62-6.84 (m, 6H), 5.67-5.27 (m, 2H), 5.16 (t, *J* = 7.0  
42  
43 Hz, 1H), 4.04-3.47 (m, 2H), 2.44-2.33 (m, 1H), 1.96-1.67 (m, 3H); LC-MS (method C, ESI, *m/z*)  
44  
45 *t*<sub>R</sub> = 1.89 min, 341/343 (M+H)<sup>+</sup>.  
46  
47  
48  
49  
50  
51  
52  
53

54 43 mg (0.13 mmol) of the racemic mixture dissolved in methanol (0.5 mL) were separated  
55  
56 into the contained enantiomerically pure materials by chiral HPLC in 25 μL/run portions  
57  
58  
59  
60

1  
2  
3 according to method C to yield in 8.9 mg (21%) of (3-amino-1*H*-indazol-5-yl)-[(2*S*)-2-(4-  
4 chlorophenyl)pyrrolidin-1-yl]methanone as a brownish solid and 8.6 mg (20%) of (3-amino-  
5 1*H*-indazol-5-yl)-[(2*R*)-2-(4-chlorophenyl)pyrrolidin-1-yl]methanone as a brownish solid.

6  
7  
8 HPLC/MS (chiral, method C): Rt 3.47 min (cpd **13**), Rt 6.45 min (cpd **ent-13**). *S*-Enantiomer:

9  
10  
11 <sup>1</sup>H NMR (500 MHz, DMSO-*d*<sub>6</sub>, mixture of rotamers) δ 11.62-11.37 (bs, 1H), 8.34-7.97 (m,  
12 1H), 7.63-6.88 (m, 6H), 5.49 (s, 2H), 5.16 (t, *J* = 7.1, 1H), 3.96-3.52 (m, 2H), 2.44-2.33 (m,  
13 1H), 1.95-1.68 (m, 3H); <sup>13</sup>C NMR (101 MHz, DMSO-*d*<sub>6</sub>, 3 signals missing) δ 169.4, 150.0,  
14 143.4, 141.6, 130.8, 128.1, 127.4, 125.9, 120.9, 113.2, 108.8, 60.1, 51.0, 34.7, 25.1; LC-MS

15  
16  
17 (method E, ESI, *m/z*) *t*<sub>R</sub> = 1.89 min, 341/343 (*M*+*H*)<sup>+</sup>. ESI-HRMS calcd for C<sub>18</sub>H<sub>18</sub><sup>35</sup>ClN<sub>4</sub>O

18  
19  
20 (*M*+*H*)<sup>+</sup>. 341.1164, found 341.1176.

21  
22  
23  
24  
25  
26  
27  
28  
29

30  
31 **(25)** [(2*S*)-2-(4-chlorophenyl)pyrrolidin-1-yl]-(3-methyl-1*H*-pyrazolo[3,4-*b*]pyridin-5-  
32 yl)methanone  
33  
34  
35

36 Into a 50 mL round bottom flask, 3-methyl-1*H*-pyrazolo[3,4-*b*]pyridine-5-carboxylic acid  
37 (0.500 g, 2.74 mmol), (*S*)-2-(4-chloro-phenyl)-pyrrolidine hydrochloride (0.720 g, 3.29 mmol),  
38  
39 *N*-(3-dimethylaminopropyl)-*N'*-ethylcarbodiimide (1.06 g, 5.48 mmol), and 1-  
40 hydroxybenzotriazole hydrate (0.380 g, 2.74 mmol) were weighed in and dissolved in *N,N*-  
41 dimethylformamide (10 mL). 4-Methylmorpholine (0.920 mL, 8.21 mmol) were added at RT  
42 and stirring was continued for 30 min at the same temperature. The mixture was poured  
43 into a mixture of brine and water (1:1, 150 mL). The resulting beige precipitate was filtered,  
44 washed with water and dried at 60 °C overnight to give 640 mg (69%) of [(2*S*)-2-(4-  
45 chlorophenyl)pyrrolidin-1-yl]-(3-methyl-1*H*-pyrazolo[3,4-*b*]pyridin-5-yl)methanone as beige  
46 solid. <sup>1</sup>H NMR (400 MHz, DMSO-*d*<sub>6</sub>) δ 13.51-13.19 (m, 1H), 8.76-6.96 (m, 6H), 5.25-4.95 (m,  
47  
48  
49  
50  
51  
52  
53  
54  
55  
56  
57  
58  
59  
60

1  
2  
3 1H), 4.03-3.51 (m, 2H), 2.62-2.28 (m, 4H), 2.00-1.68 (m, 3H); <sup>13</sup>C NMR (101 MHz, DMSO-d<sub>6</sub>,  
4  
5 1 signal missing) δ 167.3, 152.4, 148.1, 146.9, 143.0, 142.1, 130.9, 129.1, 128.1, 127.6, 124.9,  
6  
7 112.8, 60.4, 50.7, 34.8, 24.9, 12.2; LC-MS (method E, ESI, m/z) t<sub>R</sub> = 1.99 min, 341/343  
8  
9  
10 (M+H)<sup>+</sup>. ESI-HRMS calcd for C<sub>18</sub>H<sub>18</sub><sup>35</sup>ClN<sub>4</sub>O (M+H)<sup>+</sup> 341.1164, found 341.1167.  
11  
12  
13  
14  
15

16 All other experimental details (mouse, rat and human Cl<sub>int</sub> determination, Caco-2  
17  
18 determination, *In vivo* mouse PK in-life phase, *In vivo* rat & dog PK in-life phase, bioanalytics,  
19  
20 prediction of human clearance, *In vitro* cell-based reporter assays: 7dF3 Luciferase reporter  
21  
22 assay, *In vitro* biochemical assays: CDK8 Lanthascreen binding assay and reporter  
23  
24 displacement assay for CDK19, human tumour xenograft efficacy study, pharmacokinetic  
25  
26 analysis, tumor xenograft processing and Luminex analysis) are described in previous  
27  
28 publications.<sup>27,30</sup> All animal experiments were conducted in accordance with local and  
29  
30 United Kingdom National Cancer Research Institute guidelines<sup>48</sup>.  
31  
32  
33  
34  
35  
36  
37  
38

## 39 ASSOCIATED CONTENT

### 40 41 Supporting Information

42  
43  
44 The Supporting Information is available free of charge on the ACS Publications website at

45  
46  
47 [http://dx.doi.org/FILLED\\_OUT\\_LATER](http://dx.doi.org/FILLED_OUT_LATER)  
48  
49

### 50 Synthesis protocols & analytical data

51  
52  
53 **Table 1** Crystallographic data of compounds **6**, **17** and **25**  
54

55  
56 **Table 2** Kinase selectivity data of compounds **13** and **25**  
57  
58  
59  
60

1  
2  
3 **Table 3** *In vitro* pharmacology: binding assays. Activity of compound **25** tested at 10  $\mu$ M across a  
4 panel of 59 receptors and ion channels (CEREP). Results are expressed as percent inhibition of control  
5 specific binding.  
6  
7  
8  
9

10 **Figure 1** Omit maps  
11

### 12 **Accession Codes**

13  
14  
15  
16 Atomic coordinates and structure factors for the crystal structures of CDK8/cyclin C with  
17 compounds **6**, **17**, and **25** can be accessed using PDB codes 5ICP, 5IDP, and 5IDN,  
18 respectively.  
19  
20  
21  
22  
23  
24  
25  
26

### 27 **ACKNOWLEDGMENT**

28  
29  
30 We thank Dr Amin Mirza, Mr Meirion Richards and Dr Maggie Liu for their assistance with  
31 NMR, mass spectrometry and HPLC and Mr Gary Nugent and Dr Christian Herhaus for  
32 cheminformatics support. We thank the team of Proteros Biostructures GmbH,  
33 Bunsenstrasse 7a, D-82152 Martinsried, Germany for the Reporter Displacement Assay and  
34 in particular Dr Elisabeth V. Schneider and Dr Alfred Lammens for the X-ray crystal structures  
35 with CDK8/CyclinC.  
36  
37  
38  
39  
40  
41  
42  
43  
44

### 45 **Author Contributions**

46  
47  
48 The manuscript was written with contributions of all authors. All authors have given  
49 approval to the final version of the manuscript.  
50  
51  
52

### 53 **Funding Sources**

1  
2  
3 This work was supported by Cancer Research UK [grant number C309/A11566]. We  
4  
5 acknowledge NHS funding to the NIHR Biomedical Research Centre at The Institute of Cancer  
6  
7 Research and The Royal Marsden.  
8  
9

## 10 11 12 13 14 **ABBREVIATIONS**

15  
16  
17 CDK, cyclin-dependent kinase; Cl, clearance;  $CL_{int}$ , Intrinsic clearance; ER, Efflux ratio; F,  
18  
19 bioavailability; GSK3alpha, glycogen synthase kinase 3alpha; Papp Apparent permeability  
20  
21 coefficient;  $t_{1/2}$ , half life;  $V_{DSS}$ , Apparent volume of distribution at steady state; vdW, van der  
22  
23  
24 Waals;  
25  
26  
27  
28  
29  
30  
31  
32

## 33 34 **REFERENCES**

- 35  
36  
37 (1) Tsutsui, T.; Fukasawa, R.; Tanaka, A.; Hirose, Y.; Okhuma, Y. Identification of Target  
38 Genes for the CDK Subunits of the Mediator Complex. *Genes Cells* **2011**, *16* (12),  
39 1208–1218.  
40  
41 (2) Galbraith, M. D.; Donner, A. J.; Espinosa, J. M. CDK8: A Positive Regulator of  
42 Transcription. *Transcription* *1* (1), 4–12.  
43  
44 (3) Firestein, R.; Hahn, W. C. Revving the Throttle on an Oncogene: CDK8 Takes the  
45 Driver Seat. *Cancer Res.* **2009**, *69* (20), 7899–7901.  
46  
47 (4) Taatjes, D. J. The Human Mediator Complex: A Versatile, Genome-Wide Regulator of  
48 Transcription. *Trends Biochem. Sci.* **2010**, *35* (6), 315–322.  
49  
50 (5) Allen, B. L.; Taatjes, D. J. The Mediator Complex: A Central Integrator of  
51 Transcription. *Nat. Rev. Mol. Cell Biol.* **2015**, *16* (3), 155–166.  
52  
53 (6) Kim, S.; Xu, X.; Hecht, A.; Boyer, T. G. Mediator Is a Transducer of Wnt/beta-Catenin  
54 Signaling. *J. Biol. Chem.* **2006**, *281* (20), 14066–14075.  
55  
56 (7) Schiano, C.; Casamassimi, A.; Rienzo, M.; de Nigris, F.; Sommese, L.; Napoli, C.  
57  
58  
59  
60

- 1  
2  
3 Involvement of Mediator Complex in Malignancy. *Biochim. Biophys. Acta* **2014**, *1845*  
4 (1), 66–83.  
5  
6 (8) Rickert, P.; Seghezzi, W.; Shanahan, F.; Cho, H.; Lees, E. Cyclin C/CDK8 Is a Novel  
7 CTD Kinase Associated with RNA Polymerase II. *Oncogene* **1996**, *12* (12), 2631–  
8 2640.  
9  
10 (9) Bancerek, J.; Poss, Z. C.; Steinparzer, I.; Sedlyarov, V.; Pfaffenwimmer, T.; Mikulic,  
11 I.; Dölken, L.; Strobl, B.; Müller, M.; Taatjes, D. J.; Kovarik, P. CDK8 Kinase  
12 Phosphorylates Transcription Factor STAT1 to Selectively Regulate the Interferon  
13 Response. *Immunity* **2013**, *38* (2), 250–262.  
14  
15 (10) Morris, E. J.; Ji, J.-Y.; Yang, F.; Di Stefano, L.; Herr, A.; Moon, N.-S.; Kwon, E.-J.;  
16 Haigis, K. M.; Näär, A. M.; Dyson, N. J. E2F1 Represses Beta-Catenin Transcription  
17 and Is Antagonized by Both pRB and CDK8. *Nature* **2008**, *455* (7212), 552–556.  
18  
19 (11) Zhao, J.; Ramos, R.; Demma, M. CDK8 Regulates E2F1 Transcriptional Activity  
20 through S375 Phosphorylation. *Oncogene* **2013**, *32* (30), 3520–3530.  
21  
22 (12) Fryer, C. J.; White, J. B.; Jones, K. A. Mastermind Recruits CycC:CDK8 to  
23 Phosphorylate the Notch ICD and Coordinate Activation with Turnover. *Mol. Cell*  
24 **2004**, *16* (4), 509–520.  
25  
26 (13) Alarcón, C.; Zaromytidou, A.-I.; Xi, Q.; Gao, S.; Yu, J.; Fujisawa, S.; Barlas, A.;  
27 Miller, A. N.; Manova-Todorova, K.; Macias, M. J.; Sapkota, G.; Pan, D.; Massagué, J.  
28 Nuclear CDKs Drive Smad Transcriptional Activation and Turnover in BMP and TGF-  
29 Beta Pathways. *Cell* **2009**, *139* (4), 757–769.  
30  
31 (14) Zhao, X.; Feng, D.; Wang, Q.; Abdulla, A.; Xie, X.-J.; Zhou, J.; Sun, Y.; Yang, E. S.;  
32 Liu, L.-P.; Vaitheesvaran, B.; Bridges, L.; Kurland, I. J.; Strich, R.; Ni, J.-Q.; Wang,  
33 C.; Ericsson, J.; Pessin, J. E.; Ji, J.-Y.; Yang, F. Regulation of Lipogenesis by Cyclin-  
34 Dependent Kinase 8-Mediated Control of SREBP-1. *J. Clin. Invest.* **2012**, *122* (7),  
35 2417–2427.  
36  
37 (15) Adler, A. S.; McClelland, M. L.; Truong, T.; Lau, S.; Modrusan, Z.; Soukup, T. M.;  
38 Roose-Girma, M.; Blackwood, E. M.; Firestein, R. CDK8 Maintains Tumor  
39 Dedifferentiation and Embryonic Stem Cell Pluripotency. *Cancer Res.* **2012**, *72* (8),  
40 2129–2139.  
41  
42 (16) Firestein, R.; Bass, A. J.; Kim, S. Y.; Dunn, I. F.; Silver, S. J.; Guney, I.; Freed, E.;  
43 Ligon, A. H.; Vena, N.; Ogino, S.; Chheda, M. G.; Tamayo, P.; Finn, S.; Shrestha, Y.;  
44 Boehm, J. S.; Jain, S.; Bojarski, E.; Mermel, C.; Barretina, J.; Chan, J. A.; Baselga, J.;  
45 Tabernero, J.; Root, D. E.; Fuchs, C. S.; Loda, M.; Shivdasani, R. A.; Meyerson, M.;  
46 Hahn, W. C. CDK8 Is a Colorectal Cancer Oncogene That Regulates Beta-Catenin  
47 Activity. *Nature* **2008**, *455* (7212), 547–551.  
48  
49 (17) Firestein, R.; Shima, K.; Nosh, K.; Irahara, N.; Baba, Y.; Bojarski, E.; Giovannucci,  
50 E. L.; Hahn, W. C.; Fuchs, C. S.; Ogino, S. CDK8 Expression in 470 Colorectal  
51  
52  
53  
54  
55  
56  
57  
58  
59  
60

- 1  
2  
3 Cancers in Relation to Beta-Catenin Activation, Other Molecular Alterations and  
4 Patient Survival. *Int. J. Cancer* **2010**, *126* (12), 2863–2873.
- 5  
6 (18) Kapoor, A.; Goldberg, M. S.; Cumberland, L. K.; Ratnakumar, K.; Segura, M. F.;  
7 Emanuel, P. O.; Menendez, S.; Vardabasso, C.; Leroy, G.; Vidal, C. I.; Polsky, D.;  
8 Osman, I.; Garcia, B. A.; Hernando, E.; Bernstein, E. The Histone Variant macroH2A  
9 Suppresses Melanoma Progression through Regulation of CDK8. *Nature* **2010**, *468*  
10 (7327), 1105–1109.
- 11  
12  
13 (19) Fryer, C. J.; White, J. B.; Jones, K. A. Mastermind Recruits CycC:CDK8 to  
14 Phosphorylate the Notch ICD and Coordinate Activation with Turnover. *Mol. Cell*  
15 **2004**, *16* (4), 509–520.
- 16  
17  
18 (20) Li, N.; Zhu, R.; Zhang, Y. A Strong Tracking Square Root CKF Algorithm Based on  
19 Multiple Fading Factors for Target Tracking. In *2014 Seventh International Joint*  
20 *Conference on Computational Sciences and Optimization*; IEEE, 2014; pp 16–20.
- 21  
22  
23 (21) Porter, D. C.; Farmaki, E.; Altiglia, S.; Schools, G. P.; West, D. K.; Chen, M.; Chang,  
24 B.-D.; Puzyrev, A. T.; Lim, C.; Rokow-Kittell, R.; Friedhoff, L. T.; Papavassiliou, A.  
25 G.; Kalurupalle, S.; Hurteau, G.; Shi, J.; Baran, P. S.; Gyorffy, B.; Wentland, M. P.;  
26 Broude, E. V.; Kiaris, H.; Roninson, I. B. Cyclin-Dependent Kinase 8 Mediates  
27 Chemotherapy-Induced Tumor-Promoting Paracrine Activities. *Proc. Natl. Acad. Sci.*  
28 *U. S. A.* **2012**, *109* (34), 13799–13804.
- 29  
30  
31 (22) Westerling, T.; Kuuluvainen, E.; Mäkelä, T. P. Cdk8 Is Essential for Preimplantation  
32 Mouse Development. *Mol. Cell. Biol.* **2007**, *27* (17), 6177–6182.
- 33  
34 (23) Kim, M.-Y.; Han, S. I.; Lim, S.-C. Roles of Cyclin-Dependent Kinase 8 and  $\beta$ -Catenin  
35 in the Oncogenesis and Progression of Gastric Adenocarcinoma. *Int. J. Oncol.* **2011**, *38*  
36 (5), 1375–1383.
- 37  
38  
39 (24) Rzymiski, T.; Mikula, M.; Wiklik, K.; Brzózka, K. CDK8 Kinase--An Emerging Target  
40 in Targeted Cancer Therapy. *Biochim. Biophys. Acta* **2015**, *1854* (10 Pt B), 1617–1629.
- 41  
42 (25) Pelish, H. E.; Liau, B. B.; Nitulescu, I. I.; Tangpeerachaikul, A.; Poss, Z. C.; Da Silva,  
43 D. H.; Caruso, B. T.; Arefolov, A.; Fadeyi, O.; Christie, A. L.; Du, K.; Banka, D.;  
44 Schneider, E. V.; Jestel, A.; Zou, G.; Si, C.; Ebmeier, C. C.; Bronson, R. T.; Krivtsov,  
45 A. V.; Myers, A. G.; Kohl, N. E.; Kung, A. L.; Armstrong, S. A.; Lemieux, M. E.;  
46 Taatjes, D. J.; Shair, M. D. Mediator Kinase Inhibition Further Activates Super-  
47 Enhancer-Associated Genes in AML. *Nature* **2015**, *526* (7572), 273–276.
- 48  
49  
50 (26) Mallinger, A.; Crumpler, S.; Pichowicz, M.; Waalboer, D.; Stubbs, M.; Adeniji-  
51 Popoola, O.; Wood, B.; Smith, E.; Thai, C.; Henley, A. T.; Georgi, K.; Court, W.;  
52 Hobbs, S.; Box, G.; Ortiz-Ruiz, M.-J.; Valenti, M.; De Haven Brandon, A.; TePoele,  
53 R.; Leuthner, B.; Workman, P.; Aherne, W.; Poeschke, O.; Dale, T.; Wienke, D.;  
54 Esdar, C.; Rohdich, F.; Raynaud, F.; Clarke, P. A.; Eccles, S. A.; Stieber, F.;  
55 Schiemann, K.; Blagg, J. Discovery of Potent, Orally Bioavailable, Small-Molecule  
56 Inhibitors of WNT Signaling from a Cell-Based Pathway Screen. *J. Med. Chem.* **2015**,  
57  
58  
59  
60

- 1  
2  
3 58 (4), 1717–1735.  
4  
5 (27) Mallinger, A.; Schiemann, K.; Rink, C.; Stieber, F.; Calderini, M.; Crumpler, S.;  
6 Stubbs, M.; Adeniji-Popoola, O.; Poeschke, O.; Busch, M.; Czodrowski, P.; Musil, D.;  
7 Schwarz, D.; Ortiz-Ruiz, M.-J.; Schneider, R.; Thai, C.; Valenti, M.; de Haven  
8 Brandon, A.; Burke, R.; Workman, P.; Dale, T.; Wienke, D.; Clarke, P. A.; Esdar, C.;  
9 Raynaud, F. I.; Eccles, S. A.; Rohdich, F.; Blagg, J. Discovery of Potent, Selective, and  
10 Orally Bioavailable Small-Molecule Modulators of the Mediator Complex-Associated  
11 Kinases CDK8 and CDK19. *J. Med. Chem.* **2016**, *59* (3), 1078–1101.  
12  
13 (28) Schiemann, K.; Mallinger, A.; Wienke, D.; Esdar, C.; Poeschke, O.; Busch, M.;  
14 Rohdich, F.; Eccles, S. A.; Schneider, R.; Raynaud, F. I.; Czodrowski, P.; Musil, D.;  
15 Schwarz, D.; Urbahns, K.; Blagg, J. Discovery of Potent and Selective CDK8  
16 Inhibitors from an HSP90 Pharmacophore. *Bioorg. Med. Chem. Lett.* **2016**, *26* (5),  
17 1443–1451.  
18  
19 (29) Dale, T.; Clarke, P. A.; Esdar, C.; Waalboer, D.; Adeniji-Popoola, O.; Ortiz-Ruiz, M.-  
20 J.; Mallinger, A.; Samant, R. S.; Czodrowski, P.; Musil, D.; Schwarz, D.; Schneider,  
21 K.; Stubbs, M.; Ewan, K.; Fraser, E.; TePoele, R.; Court, W.; Box, G.; Valenti, M.; de  
22 Haven Brandon, A.; Gowan, S.; Rohdich, F.; Raynaud, F.; Schneider, R.; Poeschke, O.;  
23 Blaukat, A.; Workman, P.; Schiemann, K.; Eccles, S. A.; Wienke, D.; Blagg, J. A  
24 Selective Chemical Probe for Exploring the Role of CDK8 and CDK19 in Human  
25 Disease. *Nat. Chem. Biol.* **2015**, *11* (12), 973–980.  
26  
27 (30) Mallinger, A.; Schiemann, K.; Rink, C.; Sejberg, J.; Honey, M. A.; Czodrowski, P.;  
28 Stubbs, M.; Poeschke, O.; Busch, M.; Schneider, R.; Schwarz, D.; Musil, D.; Burke,  
29 R.; Urbahns, K.; Workman, P.; Wienke, D.; Clarke, P. A.; Raynaud, F. I.; Eccles, S.  
30 A.; Esdar, C.; Rohdich, F.; Blagg, J. 2,8-Disubstituted-1,6-Naphthyridines and 4,6-  
31 Disubstituted-Isoquinolines with Potent, Selective Affinity for CDK8/19. *ACS Med.*  
32 *Chem. Lett.* **2016**, acsmedchemlett.6b00022.  
33  
34 (31) Ewan, K.; Pajak, B.; Stubbs, M.; Todd, H.; Barbeau, O.; Quevedo, C.; Botfield, H.;  
35 Young, R.; Ruddle, R.; Samuel, L.; Battersby, A.; Raynaud, F.; Allen, N.; Wilson, S.;  
36 Latinkic, B.; Workman, P.; McDonald, E.; Blagg, J.; Aherne, W.; Dale, T. A Useful  
37 Approach to Identify Novel Small-Molecule Inhibitors of Wnt-Dependent  
38 Transcription. *Cancer Res.* **2010**, *70* (14), 5963–5973.  
39  
40 (32) *SZMAP 1.2*; OpenEye Scientific Software: Santa Fe, NM, 2013.  
41  
42 (33) Abel, R.; Young, T.; Farid, R.; Berne, B. J.; Friesner, R. A. Role of the Active-Site  
43 Solvent in the Thermodynamics of Factor Xa Ligand Binding. *J. Am. Chem. Soc.* **2008**,  
44 *130* (9), 2817–2831.  
45  
46 (34) Baker, N. A. Improving Implicit Solvent Simulations: A Poisson-Centric View. *Curr.*  
47 *Opin. Struct. Biol.* **2005**, *15* (2), 137–143.  
48  
49 (35) Koehl, P. Electrostatics Calculations: Latest Methodological Advances. *Curr. Opin.*  
50 *Struct. Biol.* **2006**, *16* (2), 142–151.  
51  
52  
53  
54  
55  
56  
57  
58  
59  
60



- 1  
2  
3 (36) Mortier, J.; Rakers, C.; Bermudez, M.; Murgueitio, M. S.; Riniker, S.; Wolber, G. The  
4 Impact of Molecular Dynamics on Drug Design: Applications for the Characterization  
5 of Ligand-Macromolecule Complexes. *Drug Discov. Today* **2015**, *20* (6), 686–702.  
6  
7 (37) Lazaridis, T. Inhomogeneous Fluid Approach to Solvation Thermodynamics. 1.  
8 Theory. *J. Phys. Chem. B* **1998**, *102* (18), 3531–3541.  
9  
10 (38) Czodrowski, P.; Hölzemann, G.; Barnickel, G.; Greiner, H.; Musil, D. Selection of  
11 Fragments for Kinase Inhibitor Design: Decoration Is Key. *J. Med. Chem.* **2015**, *58* (1),  
12 457–465.  
13  
14 (39) Kohlmann, A.; Zhu, X.; Dalgarno, D. Application of MM-GB/SA and WaterMap to  
15 SRC Kinase Inhibitor Potency Prediction. *ACS Med. Chem. Lett.* **2012**, *3* (2), 94–99.  
16  
17 (40) Abel, R.; Young, T.; Farid, R.; Berne, B. J.; Friesner, R. A. Role of the Active-Site  
18 Solvent in the Thermodynamics of Factor Xa Ligand Binding. *J. Am. Chem. Soc.* **2008**,  
19 *130* (9), 2817–2831.  
20  
21 (41) Robinson, D. D.; Sherman, W.; Farid, R. Understanding Kinase Selectivity through  
22 Energetic Analysis of Binding Site Waters. *ChemMedChem* **2010**, *5* (4), 618–627.  
23  
24 (42) Bortolato, A.; Tehan, B. G.; Bodnarchuk, M. S.; Essex, J. W.; Mason, J. S. Water  
25 Network Perturbation in Ligand Binding: Adenosine A(2A) Antagonists as a Case  
26 Study. *J. Chem. Inf. Model.* **2013**, *53* (7), 1700–1713.  
27  
28 (43) Grädler, U.; Czodrowski, P.; Tsaklakidis, C.; Klein, M.; Werkmann, D.; Lindemann,  
29 S.; Maskos, K.; Leuthner, B. Structure-Based Optimization of Non-Peptidic Cathepsin  
30 D Inhibitors. *Bioorg. Med. Chem. Lett.* **2014**, *24* (17), 4141–4150.  
31  
32 (44) Bayden, A. S.; Moustakas, D. T.; Joseph-McCarthy, D.; Lamb, M. L. Evaluating Free  
33 Energies of Binding and Conservation of Crystallographic Waters Using SZMAP. *J.*  
34 *Chem. Inf. Model.* **2015**, *55* (8), 1552–1565.  
35  
36 (45) Zoidis, G.; Giannakopoulou, E.; Stevaert, A.; Frakolaki, E.; Myriantopoulos, V.;  
37 Fytas, G.; Mavromara, P.; Mikros, E.; Bartenschlager, R.; Vassilaki, N.; Naesens, L.  
38 Novel Indole–flutimide Heterocycles with Activity against Influenza PA Endonuclease  
39 and Hepatitis C Virus. *Med. Chem. Commun.* **2016**, *7* (3), 447–456.  
40  
41 (46) Volkamer, A.; Eid, S.; Turk, S.; Rippmann, F.; Fulle, S. Identification and  
42 Visualization of Kinase-Specific Subpockets. *J. Chem. Inf. Model.* **2016**, *56* (2), 335–  
43 346.  
44  
45 (47) Neumann, L.; von König, K.; Ullmann, D. HTS Reporter Displacement Assay for  
46 Fragment Screening and Fragment Evolution toward Leads with Optimized Binding  
47 Kinetics, Binding Selectivity, and Thermodynamic Signature. *Methods Enzymol.* **2011**,  
48 *493*, 299–320.  
49  
50 (48) Workman, P.; Aboagye, E. O.; Balkwill, F.; Balmain, A.; Bruder, G.; Chaplin, D. J.;  
51 Double, J. A.; Everitt, J.; Farningham, D. A. H.; Glennie, M. J.; Kelland, L. R.;  
52  
53  
54  
55  
56  
57  
58  
59  
60

1  
2  
3 Robinson, V.; Stratford, I. J.; Tozer, G. M.; Watson, S.; Wedge, S. R.; Eccles, S. A.;  
4 Committee of the National Cancer Research Institute. Guidelines for the Welfare and  
5 Use of Animals in Cancer Research. *Br. J. Cancer* **2010**, *102* (11), 1555–1577.  
6  
7  
8  
9  
10  
11  
12  
13  
14  
15  
16  
17  
18  
19  
20  
21  
22  
23  
24  
25  
26  
27  
28  
29  
30  
31  
32  
33  
34  
35  
36  
37  
38  
39  
40  
41  
42  
43  
44  
45  
46  
47  
48  
49  
50  
51  
52  
53  
54  
55  
56  
57  
58  
59  
60

## Table of Contents graphic

